Available online at www.sciencedirect.com
SCIENCE DIRECT®
Journal of Computational Physics 196 (2004) 417–447
JOURNAL OF COMPUTATIONAL PHYSICS
www.elsevier.com/locate/jcp

FEM-simulation of laminar flame propagation. I: Two-dimensional flames

B. Michaelis, B. Rogg *

Lehrstuhl für Strömungsmechanik, Institut für Thermo- und Fluiddynamik, Ruhr-Universität Bochum, D-44780 Bochum, Germany

Received 9 September 2002; received in revised form 29 October 2003; accepted 30 October 2003

Abstract

In this paper, we present a numerical model for two-dimensional low-Mach-number flows of reactive ideal-gas mixtures based on the fundamental conservation equations in primitive variables. Chemical reaction is described by a detailed mechanism of elementary reactions, and detailed models for molecular transport and thermodynamics are taken into account. The equations are discretized by a finite-element method on unstructured grids using the well known Taylor–Hood element. A streamline-diffusion upwinding technique is used to avoid instabilities in convection-dominated regions of the flowfield. A fully operative local adaptive mesh-refinement procedure is used. As numerical examples we consider *steadily* propagating laminar flames in flat channels, which appear in a variety of shapes depending on the boundary conditions.

PACS: 02.70.DL; 82.40.Py

Keywords: Low-Mach-number gaseous flow; Chemical reactive flow; Finite elements; Upwinding; Streamline diffusion; Adaptive gridding

1. Introduction

Since the advent of the computer, numerical studies of laminar flames have been important for various reasons: (1) to obtain enhanced insight into the complex physical and chemical structure of these flames, (2) to provide numerical data for related experimental and theoretical investigations, (3) to develop, test and validate physical models, e.g. for full or reduced chemical kinetic mechanisms, radiation models, soot models etc., (4) to study details of the temporal and spatial structure of turbulent flames in the laminar-flamelet regime and (5) to develop, test and validate numerical methods and algorithms suitable for combustion problems. Over the years, the latter point has been addressed by numerous authors – it also is the main objective of the present work.

* Corresponding author. Tel.: +49-234-53-25914; fax: +49-234-32-14162.
E-mail address: lstm@lstm.ruhr-uni-bochum.de (B. Rogg).
URL: http://www.lstm.ruhr-uni-bochum.de.

0021-9991/$ - see front matter
doi:10.1016/j.jcp.2003.10.033

Nomenclature

c_p	Frozen specific heat at a constant pressure for the gas mixture, J/(kg K)
c_{pi}	Frozen specific heat at a constant pressure for species i, J/(kg K)
$\boldsymbol{D}_T$	Diffusion tensor in the energy equation, J/(m K s)
D_i	Mixture-averaged diffusion coefficient for species i, m^2/s
D_{ij}	Binary diffusion coefficient for species i and j, m^2/s
D_i^{T}	Thermal diffusion coefficient for species i, kg/(m s)
$\boldsymbol{e}$	Rate-of-strain tensor, Pa L
E_k	Activation energy for the kth reaction, J/mol
$\boldsymbol{g}$	External force vector per unit mass, m/s^2
G	Scaling function in the artificial upwind terms of the conservation equations
h	Mass-specific enthalpy of the gas mixture or mesh size, J/kg or m
h_i	Mass-specific enthalpy of species i, J/kg
$H^m(\Omega)$	Function space of L^2-functions with derivatives in $L^2(\Omega)$ up to mth-order
$\boldsymbol{I}$	Unit tensor
$\boldsymbol{j}_i$	Molecular diffusion-flux vector for species i, kg/(m^{2}s)
K_e	Area of the eth finite element Ω_e
$L^2(\Omega)$	Lebesque space of square-integrable functions on the computational domain Ω
M	Total number of chemical reactions, Mach number
n_k	Exponent of the temperature dependence of the frequency factor for the kth reaction
N	Total number of chemical species present
p	Pressure, Pa
p'	hydrodynamic part of p, Pa
p_0	thermodynamic part of p, Pa
p_{m}	modified pressure, Pa
P_t	Set of tth-order polynomials
$\boldsymbol{q}$	Molecular heat-flux vector, J/(m^{2}s)
R^0	Universal gas constant, J/(mol K)
$\boldsymbol{s}$	Surface traction vector, Pa m
$S,\ S(t)$	speed of the moving (Galilean) frame of reference, m/s
$S_{\mathrm{G}} = \lvert S(\infty)\rvert$	Global speed of a steadily propagating flame, m/s
S_{L}	Laminar flame speed, m/s
t	Time, s
T	Temperature, K
$\boldsymbol{v}$	Velocity vector of the gas mixture with components u, v, w in x, y, z-direction, m/s
V	Function space
$\boldsymbol{V}_i$	Diffusion velocity of species i, m/s
$\boldsymbol{V}_i^{\mathrm{T}}$	Thermal diffusion velocity of species i, m/s
w_i	Rate of production of species i by chemical reactions, kg/(m^{3}s)
$\overline{W}$	Mixture molecular weight, kg/mol
W_i	Molecular weight of species i, kg/mol
X_i	Mole fraction of species i
Y_i	Mass fraction of species i
Γ	Boundary of the computational domain
η	Global error indicator

η_e	Local error indicator on element Ω_e
λ	Thermal conductivity of the gas mixture, J/(m K s)
λ_i	Thermal conductivity of species i, J/(m K s)
μ	Coefficient of (shear) viscosity of the gas mixture, Pa s
μ_i	Coefficient of (shear) viscosity of species i, Pa s
ν_{ik}	Stoichiometric coefficient for species i appearing in reaction k, $\nu_{ik} = \nu''_{ik} - \nu'_{ik}$
ν'_{ik}	Stoichiometric coefficient for species i appearing as a reactant in reaction k
ν''_{ik}	Stoichiometric coefficient for species i appearing as a product in reaction k
ρ	Density of the gas mixture, kg/m^3
ρ_i	Partial density of species i, kg/m^3
ϕ, ψ	Weight functions
Ω	Computational domain
Ω_e	eth finite element
$\boldsymbol{\sigma}$	Stress tensor, Pa
$\boldsymbol{\tau}$	viscous part of the stress tensor, Pa

Whilst today the numerical treatment of one-dimensional (1D) laminar flames can be considered standard – that of two-dimensional (2D) or even three-dimensional (3D) laminar flames cannot – at least then not if *moderately realistic* models of molecular transport and chemistry are taken into account. Originally work on 2D simulations employing detailed mechanisms of elementary reactions was put forward by Smooke and coworkers in a series of papers [1–3,5,6] which differ in the formulation of the governing equations, in the method of discretization and in the method of adaptive gridding. Due to its well-known advantages, in the early papers the streamfunction–vorticity formulation of the governing equations was favored though primitive-variable and vorticity–velocity formulations were also used. The favored discretization method was the finite-difference method (FDM). In later papers also the finite-volume method (FVM) [7–10] and the FEM (finite-element method) [14,15] were employed. In the past, simulations of diffusion flames were most popular although also premixed flames [6,11], triple flames [12,13] and ignition problems [4,16] were investigated. Table 1 summarizes distinctive details of 2D numerical simulations of laminar reactive flows based on *detailed mechanisms of elementary reactions* – these are the flows considered in the present paper. For the excessive number of publications on simulations employing simple 1-step reaction or flamesheet models, the reader is referred to the well-known sources in the literature.

Flames propagating in channels were investigated both experimentally [17,18] and numerically [18–20]. It has been observed that such flames can appear in a variety of shapes, depending on a number of different physical or geometrical effects such as local quenching, burnt-gas vortex motion, Darrieus–Landau instability, acoustics, mixture strength variations, and open or closed tube or channel ends. In the present paper flames free of any of these effects, viz., *steadily propagating* laminar flames are considered; by definition, such flames propagate in open systems, under conditions of constant and uniform thermodynamic pressure. First, for two-dimensional planar laminar low-Mach-number flows the governing equations are formulated in terms of primitive variables. Using a finite-element method based on the Taylor–Hood element, these equations are then discretized on a triangulation of the computational domain. Then the streamline-diffusion method for upwinding is described, followed by the description of the local mesh refinement strategy. After a short presentation of the numerical methods for the solution of the final difference equations, example numerical results are presented for various ozone decomposition and hydrogen-air flames. For both chemistry systems flame shapes of tulip and meniscus form are predicted.

Table 1
Major publications on the simulation of 2D reactive flows employing detailed mechanisms of elementary reactions, excluding work involving simple 1-step chemistry and flamesheet models

Formulation	Method	Element	Refinement	Flame	Refs.
Streamf.–vorticity	FD	R	U	DF	[1]
Streamf.–vorticity	FD	R	S	DF	[2]
Primitive variables	FD	R	S	DF	[3]
Primitive variables	FD	R	S	I	[4]
Vorticity–velocity	FD	R	S	DF	[5]
Vorticity–velocity	FD	R	U	DF, PF	[6]
Primitive variables	FV	R/T	–	PF, DF	[7]
Streamf.–vorticity	FV	R	U	PF	[10]
Vorticity–velocity	FD	R	S	PF	[11]
Primitive variables	FD	R	–	PTF	[12]
Primitive variables	FV	R	S	STF	[13]
Primitive variables	FE	T	U	PF, DF	[14]
Primitive variables	FE	T	U	PPF, PTF	[15]

The notation is: FD, finite differences; FV, finite volumes; FE, finite elements; R, rectangular; T, triangular; S, structured; U, unstructured; I, ignition problem; DF, diffusion flame; SPF, stabilized premixed or decomposition flame; PPF, propagating premixed or decomposition flame; STF, stabilized triple flame; PTF, propagating triple flame.

2. Governing equations

2.1. Conservation equations

The reactive flows to be considered herein are those of ideal-gas mixtures of N chemical species, occurring at low Mach numbers M. In terms of the notation summarized in the nomenclature, the relevant conservation equations (see, e.g., [21,22]) are the overall continuity equation,

$$\frac{\mathrm{D}\rho}{\mathrm{D}t} = -\rho\ \nabla\cdot\boldsymbol{v}, \tag{1}$$

the momentum equations

$$\rho\frac{\mathrm{D}\boldsymbol{v}}{\mathrm{D}t} = \nabla\cdot\sigma + \rho\boldsymbol{g}, \tag{2}$$

the species equations

$$\rho\frac{\mathrm{D}Y_i}{\mathrm{D}t} = -\nabla\cdot\boldsymbol{j}_i + w_i, \quad i = 1,\ldots,N-1, \tag{3}$$

and the energy equation (assuming a low Mach number M and hence neglecting viscous dissipation, but also neglecting radiative heat transfer and Dufour effect)

$$\rho c_p\frac{\mathrm{D}T}{\mathrm{D}t} = \frac{\mathrm{d}p_0}{\mathrm{d}t} + \nabla\cdot(\lambda\nabla T) - \nabla T\cdot\sum_{i=1}^{N} c_{pi}\boldsymbol{j}_i - \sum_{i=1}^{N} h_i w_i. \tag{4}$$

In these equations, $\mathrm{D}/\mathrm{D}t$ denotes the substantial derivative. Assuming Newton's law of viscosity and Stokes' hypothesis, the stress tensor $\boldsymbol{\sigma}$ is decomposed as

$$\boldsymbol{\sigma} = -p_{\mathrm{m}}\boldsymbol{I} + 2\mu\boldsymbol{e}. \tag{5}$$

Here $\boldsymbol{e}$ is the rate-of-strain tensor and p_{m} is defined as $p_{\mathrm{m}} := p' - \frac{2}{3}\,\mu\nabla\cdot\boldsymbol{v}$; $p' := p - p_0$ denotes the hydrodynamic part of pressure which, in the absence of acoustic effects, is of the order of M^2. The pressure p_0 is a function of only time; it is also referred to as the thermodynamic (part of) pressure, and it is the leading term in a series expansion of pressure with M as small expansion parameter [24].

In the diffusion flux of species i, $\boldsymbol{j}_i = \rho Y_i \boldsymbol{V}_i$, the diffusion velocity $\boldsymbol{V}_i$ is taken to be of the Fickian type, i.e., $\boldsymbol{V}_i = -D_i\ \nabla(\ln X_i)$. Hence

$$\boldsymbol{j}_i = -\rho D_i(W_i/\overline{W})\nabla X_i = -\rho D_i\big(\nabla Y_i + Y_i\ \nabla(\ln\overline{W})\big), \tag{6}$$

$i = 1,\ldots,N$; here $\overline{W}$ is the mixture molecular weight,

$$\overline{W} = \left(\sum_{i=1}^{N}\frac{Y_i}{W_i}\right)^{-1}. \tag{7}$$

The mass rate of production of species i, w_i, is

$$w_i = W_i\sum_{k=1}^{M}(\nu''_{ik} - \nu'_{ik})\prod_{j=1}^{N}\left(\frac{\rho Y_j}{W_j}\right)^{\nu'_{jk}} k_k(T), \quad i = 1,\ldots,N-1 \tag{8}$$

with the rate constants k_k of the Arrhenius-type,

$$k_k = \mathrm{A}\mathrm{T}^n\exp\left(-\frac{E_k}{R^0 T}\right), \tag{9}$$

$c_p = \sum_{i=1}^{N} Y_i c_{pi}$ is the frozen constant-pressure specific heat of the mixture; p_0 denotes the spatially uniform thermodynamic pressure. The system of equations is closed by the ideal-gas thermal equation of state,

$$\rho = p_0\overline{W}/(R^0 T). \tag{10}$$

Note that the mass fraction of species N, say, is given by $Y_{\mathrm{N}} = 1 - \sum_{i=1}^{N-1} Y_i$; hence there are only $N-1$ species Eq. (3). Also note that transport coefficients and thermodynamic data are taken as variable – details are outlined in Appendix A.

The assumption of low Mach number explicitly manifests itself in (4) and (10) – in (4) by the term $\mathrm{d}p_0/\mathrm{d}t$ (which has replaced $\mathrm{D}p/\mathrm{D}t$) and by the absence of the viscous dissipation function, in (10) by p_0 (which has replaced p). What, as a consequence of the assumption, should generally be added [23–25] is an ordinary differential equation for the generally unknown p_0. However, for the open systems considered herein, this equation reduces to $\mathrm{d}p_0/\mathrm{d}t = 0$ and, therefore, p_0 is taken as a known constant.

For given constant p_0, the governing Eqs. (1)–(4) form a hybrid hyperbolic-parabolic system of $N+3$ partial differential equations for the $N+3$ unknowns p', the two velocity components, T, and $Y_1,\ldots,Y_{N-1}$, with the density ρ being viewed as a known function of these variables.

2.2. Other models

In the context of the model presented herein – and in all those models of Table 1 that are formulated in primitive variables and in which the low or zero Mach number approximation is employed –, the governing equations to be discretized and numerically solved are (1)–(4).

At this stage it is interesting and relevant to put low or zero Mach number models into a historical perspective. It has been known for a long time that for reactive flows at low Mach numbers the thermodynamic pressure, p_0, can be taken as spatially uniform [21,27]. Rehm and Baum [23] were the first to derive an ordinary differential equation for p_0 thereby enabling that quantity to be calculated on theoretically

sound grounds. Their approach was adopted by Majda [24,25] who – as others, see e.g. [26] –, employed a Helmholtz splitting of the velocity field and furthermore considered acoustic effects.

In the model used by us and others, p_0 would have to be determined from the same exact equation as in the Rehm model (but here of course incorporating detailed models for thermodynamics, molecular transport and chemistry) or, depending on the particular application, by some physically reasonable approximation. For the open systems considered herein, the Rehm equation for p_0 reduces to $\mathrm{d}p_0/\mathrm{d}t = 0$ from which $p_0 = constant$ is obtained.

2.3. Galilei transformation

In the present paper numerical solutions for steadily propagating flames are sought. By definition, for such flames the flame structure as a whole propagates in a certain well-defined direction, and both the structure itself and its propagation velocity are independent of the initial conditions. For numerical simulations of such flames it is advantageous to subject the governing equations to a Galilei transformation, and to solve the resulting (still time dependent) equations until in the Galilean frame of reference a steady state is reached.

Inherently, problems in laminar-flame propagation are transient problems. From a numerical point of view, they can efficiently be handled with a Galilei transformation. For instance, in terms of the original coordinates x, y, z, t and in terms of new coordinates x', y', z', t', a Galilei transformation for a flame propagating in the (positive or negative) x-direction is given by

$$(x', y', z', t') = \left(x - \int_0^t S\mathrm{d}t, y, z, t\right) \quad \text{and} \quad (u', v', w') = (u - S, v, w), \tag{11}$$

here $S = S(t)$ is the speed with which the Galilean frame of reference moves. In principle, there are no constraints on the definition of S. Yet it seems advantageous to define it such that

(a) during a computation the flame remains embedded in the Galilean computational domain, and
(b) when a state of steady flame propagation is reached ($\partial\phi/\partial t' = 0$ for all dependent variables ϕ), S should become independent of time and identical to the then unique propagation speed of the flame structure.

Obviously, if a Galilei transformation is applied to the governing equations, also the boundary and initial conditions are to be transformed according to (11). As an example, in the following important details of a Galilei transformation are outlined for a flame propagating in the negative x-direction into a mixture of fuel F and oxidizer, in a domain Ω that is left-bounded by an inlet Γ_I, right-bounded by an outlet Γ_O, top-bounded by a wall Γ_W and bottom-bounded by a line of symmetry Γ_S such that

$$\Gamma = \Gamma_\mathrm{I} \cup \Gamma_\mathrm{W} \cup \Gamma_\mathrm{S} \cup \Gamma_\mathrm{O}, \tag{12}$$

see Fig. 2 top. For this domain, consider one of the transformed species conservation equations, say, that for $i = F$ (fuel). Assuming zero diffusive mass flux across Γ and $\boldsymbol{v}' \cdot \boldsymbol{n} = 0$ along Γ_I, a macroscopic balance of species mass, carried out on Ω, straightforwardly yields

$$S = \frac{\int_{\Gamma_\mathrm{O}} \rho Y_F \left(\boldsymbol{v}' \cdot \boldsymbol{n}\right) \mathrm{d}s - \int_\Omega w_{Y_F}\, \mathrm{d}\boldsymbol{x} + \int_\Omega \frac{\partial \rho Y_F}{\partial t'}\, \mathrm{d}\boldsymbol{x}}{\int_{\Gamma_\mathrm{I}} \rho Y_F\, \mathrm{d}s} \tag{13}$$

as a natural definition for the instantaneous speed of the Galilean frame of reference and the flame structure. However, in practical simulations – at least in the initial phase where the solution is far from convergence – often meshes have been found to be too coarse for the integral $\int_\Omega w_{Y_F} \mathrm{d}\boldsymbol{x}$ to be calculated with sufficiently small discretization error resulting – in the worst case – in non-convergence of the numerical scheme. Therefore, as an alternative to (13), the speed of the Galilean frame of reference has been taken as

$$S(t) = S(t_0) + \sum_{n=1}^{\infty} (\Delta S)_n. \tag{14}$$

Here n is the number of the timestep and, for fixed $y' = y'_T$, $(\Delta S)_n$ is the time rate of shift in the x'-direction of the point (x'_T, y'_T) on a specified isotherm,

$$(\Delta S)_n = \left(\frac{\mathrm{d}x'_T}{\mathrm{d}t'} \right)_n \quad \text{for fixed } y'_T. \tag{15}$$

Note that for flames that in the limit $t' \to \infty$ propagate steadily, $\lim_{n\to\infty} (\Delta S)_n = 0$ upon overall convergence of the numerical solution, hence the above requirement (b) is fulfilled. Furthermore, inspection of the numerical results during the transient phase of the computations showed that requirement (a) was fulfilled too.

A final remark is concerned with the selection of a point on a specified isotherm as indicator of the instantaneous flame position. For the flames considered herein this choice has been found adequate. For instance in the presence of strong temporally and spatially varying heat losses, isotherms may be strongly wrinkled, bending forwards and backwards, leading to the prediction of multiple (and hence physically meaningless) flame positions. For flames under such conditions, possibly a point on an isoline of the mass fraction of a suitable chemical species could be selected to define the speed of the moving frame of reference.

Subsequently the superscript $'$ will be dropped from the dependent and independent variables, and the laboratory and the Galilean frame of reference will be distinguished from context.

2.4. Boundary conditions

The computational domain is denoted by Ω, its boundary by Γ, and the local normal and tangential unit vector on Γ by $\boldsymbol{n}$ and $\boldsymbol{t}$, respectively. The convention adopted in the following is that, (i), $\boldsymbol{n}$ points to the outside of Ω and, (ii), the direction of $\boldsymbol{t}$ corresponds to counterclockwise circumnavigation of Ω.

For all dependent variables except p' or p_m, respectively, – why pressure is excluded will be said below – provision is made for Dirichlet and non-Dirichlet boundary conditions; the latter include Neumann conditions but also certain inflow and outflow conditions as well as various other conditions that can be attributed to neither the Dirichlet nor the Neumann type. Let ϕ stand for any velocity component, for any species mass fraction or for temperature. Then, for each ϕ, Γ is decomposed into the collection of all parts on which Dirichlet conditions are imposed, Γ^ϕ_D, and into the collection of all parts on which non-Dirichlet conditions are imposed, Γ^ϕ_N, i.e.,

$$\Gamma = \Gamma^\phi_\mathrm{D} \cup \Gamma^\phi_\mathrm{N} \quad \text{and} \quad \emptyset = \Gamma^\phi_\mathrm{D} \cap \Gamma^\phi_\mathrm{N} \quad \text{for any } \phi. \tag{16}$$

Although generally different ϕ are associated with different Γ^ϕ_D and Γ^ϕ_N, for convenience of notation subsequently the superscript relating to a particular ϕ will be dropped from the Γ's.

2.4.1. Conditions for continuity and momentum equations

The formulation of a Dirichlet or Neumann condition for a velocity component v_α is straightforward, viz.,

$$v_\alpha|_{\Gamma_\mathrm{D}} = v^*_\alpha \quad \text{on } \Gamma_\mathrm{D} \tag{17}$$

or

$$\frac{\partial v_\alpha}{\partial n}|_{\Gamma_\mathrm{D}} = v^*_{\alpha,n} \quad \text{on } \Gamma_\mathrm{N}, \tag{18}$$

respectively, with v_α^* and $v_{\alpha,n}^*$ specified. Although (18) often is employed as an outflow boundary condition, generally its use is not encouraged [28]. Obviously, if locally on Γ for both velocity components v_α Dirichlet conditions are specified, then this is equivalent to specifying a Dirichlet condition for both the normal and tangential component of velocity, $v_n := \boldsymbol{v}\cdot\boldsymbol{n}$ and $v_t := \boldsymbol{v}\cdot\boldsymbol{t}$, respectively:

$$v_n = v_n^* \quad \text{and} \quad v_t = v_t^*, \quad \text{both on } \Gamma_{\mathrm{D}}. \tag{19}$$

Two further non-Dirichlet boundary conditions can be derived by considering the surface force per unit area acting locally on Γ, i.e., the product $\boldsymbol{\sigma}\cdot\boldsymbol{n}$ of the stress tensor $\boldsymbol{\sigma} = -p_{\mathrm{m}}\boldsymbol{I} + 2\mu\boldsymbol{e}$ and the normal unit vector $\boldsymbol{n}$. This surface force can readily be decomposed into components s_n and s_τ in $\boldsymbol{n}$-direction and $\boldsymbol{t}$-direction, respectively. In particular, for a piecewise planar boundary,

$$s_n = -p_{\mathrm{m}} + 2\mu\frac{\partial v_n}{\partial n} \quad \text{and} \quad s_\tau = \mu\left(\frac{\partial v_\tau}{\partial n} + \frac{\partial v_n}{\partial \tau}\right) \tag{20}$$

is obtained. Either of the two equations given in (20) – either in its own right – constitutes a non-Dirichlet boundary condition for velocity [28,29].

It is important to note that, for a specific problem at hand, care is to be taken to specify boundary conditions for the continuity and the two momentum equations such that a well-posed problem results. Various possible combinations of boundary conditions sufficient to ensure well-posedness have been discussed [28,29]. In summary, the findings relevant to the present work are:

(i) locally on Γ two boundary conditions for velocity are to be imposed as specified under (ii), (iii) and (iv);
(ii) these can be two Dirichlet conditions (17), or two Neumann conditions (18), or one Dirichlet condition (17) and one Neumann condition (18);
(iii) alternatively, these can be two conditions (20), or one Dirichlet condition (17) and one condition (20);
(iv) alternatively, in (iii), the 1st and 2nd equation in (20)can be replaced by the 1st and 2nd equation, respectively, in (19);
(v) specification of pressure on a part of Γ is to be accomplished by utilizing the 1st equation in (20).

2.4.2. Conditions for energy and species equations

For temperature, Dirichlet conditions correspond to specification of the temperature on Γ_{D}, Neumann conditions to specification of the normal component of the heat flux, $q_n = \boldsymbol{q}\cdot\boldsymbol{n} = -\lambda\partial T/\partial n$ on Γ_{N}. Similarly, for a mass fractions Y_i or for any other measure of concentration of species i, Dirichlet conditions correspond to specification of the respective concentration on Γ_{D}, Neumann conditions to the specification of the normal component of the respective diffusion flux $j_{i,n} = \boldsymbol{j}_i\cdot\boldsymbol{n}$; for the Fickian diffusion law assumed herein, see (6), $j_{i,n} = -\rho D_i(W_i/\overline{W})\partial X_i/\partial n$ on Γ_{N}.

2.4.3. Conditions for propagating flames

After the Galilei transformation has been employed, the boundary conditions for the propagating flames considered herein are at the inlet Γ_{I}:

$$u|_{\Gamma_{\mathrm{I}}} = -S, \quad v|_{\Gamma_{\mathrm{I}}} = 0, \quad T|_{\Gamma_{\mathrm{I}}} = 300\ \mathrm{K}, \quad Y_i|_{\Gamma_{\mathrm{I}}} = Y_{i,I}, \quad i = 1,\ldots,N, \tag{21}$$

at the axis of symmetry Γ_{S}:

$$\frac{\partial u}{\partial n}|_{\Gamma_{\mathrm{S}}} = 0, \quad v|_{\Gamma_{\mathrm{S}}} = 0, \quad q_n|_{\Gamma_{\mathrm{S}}} = 0, \quad j_{i,n}|_{\Gamma_{\mathrm{S}}} = 0, \quad i = 1,\ldots,N, \tag{22}$$

and at an isothermal wall Γ_{W}:

$$u|_{\Gamma_{\mathrm{W}}} = -S, \quad v|_{\Gamma_{\mathrm{W}}} = 0, \quad T|_{\Gamma_{\mathrm{W}}} = 300\ \mathrm{K}, \quad j_{i,n}|_{\Gamma_{\mathrm{W}}} = 0, \quad i = 1,\ldots,N. \tag{23}$$

In the case of an adiabatic wall, the boundary condition for the energy equation is replaced by

$$q_n|_{\Gamma_W} = -\lambda \frac{\partial T}{\partial n}|_{\Gamma_W} = 0. \tag{24}$$

At the outlet Γ_O

$$s_n|_{\Gamma_O} = -p_m + 2\mu \frac{\partial u}{\partial x} = 0, \quad \frac{\partial v}{\partial x}|_{\Gamma_O} = 0 \tag{25}$$

is specified together with homogeneous Neumann conditions for the energy equation and species equations.

2.5. Weak form of the conservation equations

The governing Eqs. (1)–(4), together with suitable boundary and initial conditions, represent an initial boundary value problem. A variational or weak formulation of this problem is obtained by multiplying each governing equation with a suitably defined weight function, say ψ or ϕ, and by integrating the resulting product over the computational domain.

It is important to note that for the governing equations alternative weak formulations exist, depending on details of the application of Green's theorem. Herein care has been taken that the individual weak formulations remain free of derivatives of transport properties and density so that, as a consequence, in the final discrete formulation cumbersome approximation and/or evaluation of such derivatives is avoided.

Division of (1) by ρ, followed by multiplication of the resulting equation by a weight function ψ and subsequent integration over Ω, yields

$$\int_\Omega \psi \left[\frac{\partial \ln \rho}{\partial t} + \nabla \cdot \boldsymbol{v} \right] \mathrm{d}\boldsymbol{x} = -\int_\Omega \psi \ \boldsymbol{v} \cdot \nabla \ln \rho \, \mathrm{d}\boldsymbol{x} \quad \forall \psi \in H^1(\Omega)$$

and hence, after partial integration,

$$\int_\Omega \psi \left[\frac{\partial \ln \rho}{\partial t} + \nabla \cdot \boldsymbol{v} \right] \mathrm{d}\boldsymbol{x} - \int_\Omega \ln \rho \nabla \cdot (\psi \boldsymbol{v}) \, \mathrm{d}\boldsymbol{x} = -\int_\Gamma \psi \ln \rho (\boldsymbol{v} \cdot \boldsymbol{n}) \, \mathrm{d}s \quad \forall \psi \in H^1(\Omega) \tag{26}$$

as a weak form of the continuity equation. In (26), H^1 is the function space with the usual meaning, see nomenclature. Similarly, a weak formulation for the momentum Eq. (2) is obtained as

$$\int_\Omega \phi \rho \left(\frac{\mathrm{D}\boldsymbol{v}}{\mathrm{D}t} - \boldsymbol{g} \right) \mathrm{d}\boldsymbol{x} + \int_\Omega \boldsymbol{\sigma} \cdot \nabla \phi \, \mathrm{d}\boldsymbol{x} = \int_\Gamma \phi \ \boldsymbol{\sigma} \cdot \boldsymbol{n} \, \mathrm{d}s \quad \forall \phi \in V^1(\Omega)$$

or with (5) and $\boldsymbol{\sigma} \cdot \boldsymbol{n} = \boldsymbol{s}$, as

$$\int_\Omega \phi \rho \left(\frac{\mathrm{D}\boldsymbol{v}}{\mathrm{D}t} - \boldsymbol{g} \right) \mathrm{d}\boldsymbol{x} - \int_\Omega p_m \nabla \phi \, \mathrm{d}\boldsymbol{x} + \int_\Omega 2\mu \boldsymbol{e} \cdot \nabla \phi \ \mathrm{d}\boldsymbol{x} = \int_\Gamma \phi \boldsymbol{s} \, \mathrm{d}s \quad \forall \phi \in V^1(\Omega). \tag{27}$$

In (27), $V^1(\Omega) := \{\phi \in H^1(\Omega) \text{ with } \phi \,|_{\Gamma_D} = 0\}$. If locally and/or instantaneously the Γ_D's of the two velocity components are not identical, then the weak formulation of the momentum equations would have to be formulated for each component separately – a trivial matter.

Weak formulations of the energy and species equations are

$$\int_\Omega \phi \left[c_p \rho \frac{\mathrm{D}T}{\mathrm{D}t} \frac{\mathrm{d}p_0}{\mathrm{d}t} - w_T + \nabla T \cdot \sum_{i=1}^{N} c_{p,i} \boldsymbol{j}_i \right] \mathrm{d}\boldsymbol{x} + \int_\Omega \lambda \nabla T \cdot \nabla \phi \, \mathrm{d}\boldsymbol{x} = \int_\Gamma \phi \lambda \nabla T \cdot \boldsymbol{n} \, \mathrm{d}s \quad \forall \phi \in V^1(\Omega) \tag{28}$$

with

$$-w_T := \sum_{i=1}^{N} h_i w_i \tag{29}$$

and

$$\int_\Omega \phi \left[\rho \frac{\mathrm{D}Y_i}{\mathrm{D}t} - w_{Y_i} \right] \mathrm{d}\boldsymbol{x} + \int_\Omega \boldsymbol{j}_i \cdot \nabla\phi \, \mathrm{d}\boldsymbol{x} = -\int_\Gamma \phi \boldsymbol{j}_i \cdot \boldsymbol{n} \, \mathrm{d}s \quad \forall \phi \in V^1(\Omega), \tag{30}$$

respectively. The weak formulation for the two-dimensional axisymmetric case is summarized in Appendix C.

2.6. Principle of upwinding and scalar equations

Herein an artificial-diffusion method is employed to suppress numerical instabilities in convection-dominated regions of the flow. Specifically, streamline diffusion [30,32] is added by disturbing the weight functions of the convective terms in the conservation equations.

First, we consider the balance of only the convective and diffusive terms in the energy Eq. (4). For simplicity of notation we restrict ourselves to the two-dimensional case but note that the generalization to three space dimensions is straightforward. In terms of an isotropic diffusion tensor

$$\boldsymbol{D}_T = \lambda \boldsymbol{I}, \tag{31}$$

(4) is written as

$$c_p \rho \boldsymbol{v} \cdot \nabla T - \nabla \cdot \boldsymbol{D}_T \nabla T = 0. \tag{32}$$

Numerical stabilization is achieved by introducing the non-isotropic artificial diffusion tensor

$$\boldsymbol{D}'_T = \frac{\lambda_k}{|\boldsymbol{v}|^2} \begin{pmatrix} u^2 & uv \\ uv & v^2 \end{pmatrix} \tag{33}$$

such that (32) renders

$$c_p \rho \boldsymbol{v} \cdot \nabla T - \nabla \cdot \left(\boldsymbol{D}_T + \boldsymbol{D}'_T \right) \nabla T = 0. \tag{34}$$

It can be shown that $\boldsymbol{D}'_T$ introduces into (34) a diffusion-like effect that locally and instantaneously acts (only and only) in the direction of the flow velocity. In (33) and hence (34), λ_k is a quantitative measure of that effect; it therefore is referred to as artificial diffusivity. With

$$\kappa_T := \lambda_k / (\rho c_p |\boldsymbol{v}|^2) \tag{35}$$

and

$$\nabla\phi \cdot \kappa_T \boldsymbol{v}\boldsymbol{v}^{\mathrm{T}} \nabla T = \kappa_T (\nabla\phi \cdot \boldsymbol{v})(\boldsymbol{v} \cdot \nabla T), \tag{36}$$

and after application of Green's theorem, we obtain as modified weak formulation of the energy equation

$$\begin{aligned} &\int_\Omega \rho c_p \boldsymbol{v} \cdot \nabla T [\phi + \kappa_T \boldsymbol{v} \cdot \nabla\phi] \, \mathrm{d}\boldsymbol{x} + \int_\Omega \nabla\phi \cdot \lambda \nabla T \, \mathrm{d}\boldsymbol{x} \\ &\quad = \int_\Gamma \phi \ \kappa_T \ \rho c_p (\boldsymbol{v} \cdot \nabla T)(\boldsymbol{v} \cdot \boldsymbol{n}) \, \mathrm{d}s + \int_\Gamma \phi \lambda \nabla T \cdot \boldsymbol{n} \, \mathrm{d}s \quad \forall \phi \in H^1(\Omega). \end{aligned} \tag{37}$$

In (37), two things are important to note which both are consequences of the application of Green's theorem. First, rather than appearing in form of a diffusion-like term, artificial diffusion manifests itself by effectively modifying the weight function of the convective term – the first term on the left hand side. Second, the first term on the right hand side is an additional boundary integral – herein this term has been found to be of paramount importance for the suppression of wiggles in predicted profiles along inflow boundaries on which non-Dirichlet conditions are imposed.

To derive a local quantitative criterion for the coefficient κ_T and hence for the artificial thermal conductivity λ_k, we write

$$\lambda_k = G_T c_p \rho h |\boldsymbol{v}|. \tag{38}$$

Here $G_T = G_T(\boldsymbol{x}, t)$ is a scaling function to be specified below and

$$h = \sqrt{K_e/\pi} \tag{39}$$

represents the local mesh size; K_e denotes the area of that triangle Ω_e that is centered about $\boldsymbol{x}$ – see Section 3, Eq. (52). The local and instantaneous magnitude of G is based on the idea that streamline diffusion should be applied only in convection-dominated regions of Ω. The usual measure for the ratio of convective to diffusive energy transport in Ω_e is the local Peclet number,

$$Pe_T(\lambda) = c_p \rho |\boldsymbol{v}| h/\lambda. \tag{40}$$

For $Pe_T \leqslant \overline{Pe}_T$, no streamline diffusion is added. For $Pe_T > \overline{Pe}_T$, λ is replaced by $\lambda + \lambda_k$ with λ_k such that $Pe_T(\lambda + \lambda_k) = \overline{Pe}_T$ or $\lambda_k = -\lambda + (c_p \rho |\boldsymbol{v}| h)/\overline{Pe}_T$, respectively. Hence, with (38),

$$G_T(\boldsymbol{x}, t) = \begin{cases} \frac{1}{\overline{Pe}_T} - \frac{1}{Pe_T(\lambda)} & \text{for} \quad Pe_T(\lambda) > \overline{Pe}_T, \\ 0 & \text{otherwise} \end{cases} \tag{41}$$

is obtained. The expression for G given in (41) has the obvious advantage to be bounded even for strong local dominance of convection when $Pe_T(\lambda) \to \infty$. What remains is the specification of the upper bound $\overline{Pe}_T$. Following the well-known reasoning for the stability of the one-dimensional convection–diffusion equation [32], herein $\overline{Pe}_{T,l} = 2$ has been selected.

It is straightforward to verify that the implementation of the streamline upwinding just described into the full energy Eq. (28) corresponds to replacing the integral $\int_\Omega \phi \rho c_p (\mathrm{D}T/\mathrm{D}t) \mathrm{d}\boldsymbol{x}$ there by

$$\int_\Omega \left(\phi \rho c_p \frac{\partial T}{\partial t} + \rho c_p \boldsymbol{v} \cdot \nabla T [\phi + \kappa_T \boldsymbol{v} \cdot \nabla \phi] \right) \mathrm{d}\boldsymbol{x} - \int_\Gamma \phi \ \kappa_T \ \rho c_p (\boldsymbol{v} \cdot \nabla T)(\boldsymbol{v} \cdot \boldsymbol{n}) \, \mathrm{d}s. \tag{42}$$

The upwind-treatment of the species conservation equations is accomplished in a manner similar that for the energy equation and hence is described only in short form. The relevant local Peclet number is

$$Pe_{Y_i}(D_i) = |\boldsymbol{v}| h / D_i, \quad i = 1, \ldots, N. \tag{43}$$

For the artificial mixture-averaged diffusion coefficient $D_{k,i}$ for species i we write

$$\rho D_{k,i} = G_{Y_i} h \rho |\boldsymbol{v}|, \tag{44}$$

and hence obtain for the scaling functions in the species mass conservation equations

$$G_{Y_i}(\boldsymbol{x}, t) = \begin{cases} \frac{1}{\overline{Pe}_{Y_i}} - \frac{1}{Pe_{Y_i}(D_i)} & \text{for} \quad Pe_{Y_i}(D_i) > \overline{Pe}_{Y_i}, \\ 0 & \text{otherwise.} \end{cases} \tag{45}$$

Here $\overline{Pe}_{Y_i}$ indicates the upper bound for the local Peclet number.

2.7. Momentum equations

In the following exemple for all three momentum equations we only consider the equation in x-direction. Consistent with (34), the modified momentum equation reads

$$\rho \boldsymbol{v} \cdot \nabla u = -\nabla p_{\mathrm{m}} + \nabla \cdot \left(2\mu \boldsymbol{e}_x + \kappa_u \boldsymbol{v}\boldsymbol{v}^{\mathrm{T}} \nabla u\right) + \rho g_x, \tag{46}$$

where

$$\boldsymbol{e}_x = \left(e_{xx}, e_{xy}\right)^{\mathrm{T}}, \quad \kappa_u = \frac{\mu_k}{|\boldsymbol{v}|^2}. \tag{47}$$

Proceeding as in the previous section, for the modified weak formulation of the momentum equation we obtain

$$\begin{aligned} &\int_\Omega \rho \boldsymbol{v} \cdot \nabla u(\phi + \kappa_u \boldsymbol{v} \cdot \nabla \phi)\,\mathrm{d}\boldsymbol{x} + \int_\Omega \left(2\mu \boldsymbol{e}_x \cdot \nabla \phi - p_{\mathrm{m}} \frac{\partial \phi}{\partial x} - \rho g_x \phi\right)\,\mathrm{d}\boldsymbol{x} \\ &\quad = \int_\Gamma \phi\ \kappa_u\ \rho(\boldsymbol{v} \cdot \nabla u)(\boldsymbol{v} \cdot \boldsymbol{n})\,\mathrm{d}s + \int_\Gamma \phi s_x \,\mathrm{d}s \quad \forall \phi \in H^1(\Omega). \end{aligned} \tag{48}$$

To obtain a local quantitative criterion for the artificial viscosity μ_k, we write

$$\mu_k = G_U \rho h |\boldsymbol{v}|, \qquad Re(\mu) = \frac{\rho |\boldsymbol{v}| h}{\mu} \tag{49}$$

with the local Reynolds number $Re(\mu)$ and

$$G_U(\boldsymbol{x}, t) = \begin{cases} \frac{1}{\overline{Re}} - \frac{1}{Re(\mu)} & \text{for} \quad Re(\mu) > \overline{Re}, \\ 0 & \text{otherwise.} \end{cases} \tag{50}$$

Here $\overline{Re}$ indicates the upper bound for the local Reynolds number.

3. Finite-element formulation

3.1. Preliminaries

On Ω, each dependent variable U, $U = u, v, p_{\mathrm{m}}, T, Y_1, \ldots, Y_{N-1}$, is approximated by a function U^h of the form

$$U^h = U_0^h + \sum_{k=1}^{M_U} \left[c_U\ \phi_U^h\right]_k. \tag{51}$$

Here $U_0^h(\Omega)$ and $\phi_{U,k}^h(\Omega)$ are the global interpolation functions to be specified; the coefficients $c_{U,k}$ are the unknowns. Specifically, $U_0^h(\Omega)$ has to be selected such that it satisfies all non-homogeneous boundary conditions that may be imposed on the variable U. For the computational domain Ω a triangulation $\mathscr{T}^h$ is defined which decomposes Ω into E triangular elements Ω_e such that

$$\Omega = \bigcup_{e=1}^{E} \Omega^e \quad \text{and} \quad \emptyset = \bigcap_{e=1}^{E} \Omega^e. \tag{52}$$

Specifically, herein for $\Omega_e \in \mathscr{T}^h$ the well-established triangular Taylor–Hood element is chosen which ensures stability as expressed in the Babuška–Brezzi condition. Thus, locally for pressure linear interpolation functions are employed and quadratic interpolation functions for all other dependent variables.

3.2. Linearization and iteration

Herein three modes of iteration are distinguished: (i) timestepping, (ii), outer iterations for the convective and reactive terms and, (iii) inner iterations for the solution of linear systems of equations. Timestepping employs simple Euler-backward differences for all transient terms except for $\partial\rho/\partial t$ – the treatment of the latter is described separately below. Outer iterations for the convective terms are Picard iterations, whereas outer iterations for the reaction terms are based on Newton iterations. Picard iterations are also employed for the density, the transport properties and the thermodynamic data.

3.2.1. Chemical source terms

The chemical source terms $w_T, w_{Y_1}, \ldots, w_{Y_{N-1}}$ are known to be strongly non-linear and stiff, and hence require linearization. Thus, in terms of the vector of scalars

$$\boldsymbol{U} = (T, Y_1, \ldots, Y_{N-1})^{\mathrm{T}}, \tag{53}$$

the source-term vector

$$\boldsymbol{w}(\boldsymbol{U}) = (w_T, w_{Y_1}, \ldots, w_{Y_{N-1}})^{\mathrm{T}} \tag{54}$$

is approximated as

$$\boldsymbol{w} \approx \boldsymbol{w}_0 + \boldsymbol{J} \cdot (\boldsymbol{U} - \boldsymbol{U}_0), \tag{55}$$

where $\boldsymbol{w}_0 = \boldsymbol{w}(\boldsymbol{U}_0)$ and where the Jacobian $\boldsymbol{J} = \boldsymbol{J}(\boldsymbol{U}_0)$ is

$$\boldsymbol{J} = \begin{pmatrix} \frac{\partial w_T}{\partial T} & \frac{\partial w_T}{\partial Y_1} & \cdots & \frac{\partial w_T}{\partial Y_{N-1}} \\ \frac{\partial w_{Y_1}}{\partial T} & \frac{\partial w_{Y_1}}{\partial Y_1} & \cdots & \frac{\partial w_{Y_1}}{\partial Y_{N-1}} \\ \vdots & & \cdots & \vdots \\ \frac{\partial w_{Y_{N-1}}}{\partial T} & \frac{\partial w_{Y_{N-1}}}{\partial Y_1} & \cdots & \frac{\partial w_{Y_{N-1}}}{\partial Y_{N-1}} \end{pmatrix}. \tag{56}$$

$\boldsymbol{U}_0$ denotes a known approximation to the vector of scalars such as the solution from the previous timestep or from the previous outer iteration.

The Jacobian $\boldsymbol{J}$ is evaluated by numerical differentiation. To reduce the number of non-zero elements in the species Jacobian matrix

$$K_{ij} := \frac{\partial w_i}{\partial Y_j}, \quad 1 \leqslant i, j \leqslant N-1, \tag{57}$$

three alternative approximations to K_{ij} have been explored, viz.,

$$K_{ij} \approx (\rho/W_j)(\partial w_i/\partial C_j), \tag{58}$$

$$K_{ij} \approx (\rho/W_j)(1 - X_j)(\partial w_i/\partial C_j), \tag{59}$$

and

$$K_{ij} \approx m_{ij}(\partial w_i/\partial Y_j) \tag{60}$$

with $m_{ij} = 0$ for $(\partial w_i/\partial C_j) = 0$ and $m_{ij} = 1$ otherwise. In the context of (60) it is important to note that the identification of zero elements m_{ij} can easily be achieved by inspection of the underlying reaction mechanism and does *not* require the evaluation of $\partial w_i/\partial C_j$. Note that although the three alternative approximations to the Jacobian are different, they have zero elements in identical locations. The derivation of the three alternatives is given in Appendix D.

3.2.2. Time-discretization

The time derivatives of all dependent variables, except that of the density ρ, are expressed in terms of backward Euler differences. The term $\partial \ln\rho/\partial t = (1/\rho)\partial\rho/\partial t$ appearing in the weak-form continuity Eq. (26) could be approximated by a backward Euler difference too, but for the *steady* solutions sought herein this appears too cumbersome. An alternative would be dropping that term completely, but this has been found to render the solution of the linear system much more difficult, resulting in long computational times. Instead, herein the term is replaced by an artificial perturbation which approaches zero upon convergence to steady propagation. To derive this perturbation, we take an approach similar to the artificial compressibility concept, see e.g. [31], p. 144. Specifically, herein in (26) the term $\partial \ln\rho/\partial t$ is replaced by

$$0 = \frac{c}{\rho}(p_{\mathrm{m}} - p_{\mathrm{m}}) \approx \frac{c}{\rho^n_{l-1}}\left(p^n_{m,l} - p^n_{m,l-1}\right), \quad l = 1, 2, \ldots. \tag{61}$$

Here c is a positive constant of dimension s/m^2, the subscript l denotes the lth Picard iteration, and the superscript n the nth timestep. Thus the modified continuity equation becomes

$$\frac{c}{\rho^n_{l-1}}\left(p^n_{m,l} - p^n_{m,l-1}\right) + \nabla\cdot\boldsymbol{v} = -\boldsymbol{v}\cdot\nabla(\ln\rho). \tag{62}$$

It is important to note that the first term on the left-hand side of (62) is of no physical significance: it is to be viewed as a perturbation that vanishes upon convergence of the Picard iterations (outer iterations), i.e., $\lim_{l\to\infty}(p^n_{m,l} - p^n_{m,l-1}) \to 0$.

The value of c is to be specified on the basis of numerical experimentation; for the problems considered herein, values in the range $\mathrm{O}(10^{-9}) \leqslant c \leqslant \mathrm{O}(10^{-5})$ s/m^2 have been found to work well. In particular, for c in this range, the first term on the left-hand side of (62) has been found to have no influence, neither on the number of Picard iterations nor on the number of timesteps required to obtain a steady solution. Furthermore we have found that if the first term on the left-hand side of (62) is dropped, then the BCGSTAB linear-system solver requires substantially more – sometimes excessive many – iterations.

3.3. Assembly

In terms of the overall vector of unknowns, $\mathscr{U} = (\mathscr{U}_{\boldsymbol{v}}, \mathscr{U}_T)^{\mathrm{T}}$ where $\mathscr{U}_{\boldsymbol{v}} = (\boldsymbol{u}, \boldsymbol{v}, \boldsymbol{p})^{\mathrm{T}}$ and $\mathscr{U}_T = (\boldsymbol{T}, \boldsymbol{Y}_1, \ldots, \boldsymbol{Y}_{N-1})^{\mathrm{T}}$, the overall linear system to be solved is

$$\boldsymbol{A}\cdot\mathscr{U} = \boldsymbol{b}. \tag{63}$$

Since for the density Picard iterations are employed, $\boldsymbol{A}$ is diagonal,

$$\boldsymbol{A} = \begin{pmatrix} \boldsymbol{A}_{\boldsymbol{v}} & \boldsymbol{0} \\ \boldsymbol{0} & \boldsymbol{A}_T \end{pmatrix}. \tag{64}$$

As a consequence, the overall linear system (63) can be decomposed into a fluidmechanical and a thermochemical subsystem, viz.,

$$\boldsymbol{A}_{\boldsymbol{v}}\cdot\mathscr{U}_{\boldsymbol{v}} = \boldsymbol{b}_{\boldsymbol{v}} \quad \text{and} \quad \boldsymbol{A}_T\cdot\mathscr{U}_T = \boldsymbol{b}_T. \tag{65}$$

Here

$$A_{\boldsymbol{v}} = \begin{pmatrix} \boldsymbol{A}^{uu} & \boldsymbol{A}^{uv} & \boldsymbol{A}^{up} \\ \boldsymbol{A}^{vu} & \boldsymbol{A}^{vv} & \boldsymbol{A}^{vp} \\ \boldsymbol{A}^{pu} & \boldsymbol{A}^{pv} & \boldsymbol{A}^{pp} \end{pmatrix} \tag{66}$$

and

$$A_T = \begin{pmatrix} \boldsymbol{A}^{TT} & \boldsymbol{A}^{TY_1} & \cdots & \boldsymbol{A}^{TY_{N-1}} \\ \boldsymbol{A}^{Y_1T} & \boldsymbol{A}^{Y_1Y_1} & \cdots & \boldsymbol{A}^{Y_1Y_{N-1}} \\ \vdots & \vdots & \cdots & \vdots \\ \boldsymbol{A}^{Y_{N-1}T} & \boldsymbol{A}^{Y_{N-1}Y_1} & \cdots & \boldsymbol{A}^{Y_{N-1}Y_{N-1}} \end{pmatrix}. \tag{67}$$

The advantage of (65) over (63) is twofold. First, although with the BCGSTAB solver the total number of iterations remains essentially unchanged, with (65) the computational cost per iteration step is substantially reduced. Second, the formulation in (65) allows an effective splitting of operators by solving the fluidmechanical and thermochemical subsystems in succession. Within each subsystem or block, the governing equations are solved simultaneously, i.e., the Picard approximations are applied simultaneously to all equations pertaining to a block.

The linear subsystems (65) have been obtained by the usual assembly procedure according to which $\boldsymbol{A}_{\boldsymbol{v}} = \sum_{e=1}^{E} \boldsymbol{A}_{\boldsymbol{v},e}$, $\boldsymbol{b}_{\boldsymbol{v}} = \sum_{e=1}^{E} \boldsymbol{b}_{\boldsymbol{v},e}$, $\boldsymbol{A}_T = \sum_{e=1}^{E} \boldsymbol{A}_{T,e}$ and $\boldsymbol{b}_T = \sum_{e=1}^{E} \boldsymbol{b}_{T,e}$; here it is understood that the element matrices and vectors are properly augmented by zeroes. The element matrices $\boldsymbol{A}_{\boldsymbol{v},e}$ and $\boldsymbol{A}_{T,e}$ have the same structure as (66) and (67), respectively; the corresponding element linear systems have the same form as (64).

A further point is noteworthy. The element submatrices $\boldsymbol{A}_e^{TY_i}$ and $\boldsymbol{A}_e^{Y_iY_j}$ with $i \neq j$ of $\boldsymbol{A}_{T,e}$ - and hence the corresponding submatrices of the system matrix $\boldsymbol{A}_T$ – are non-zero only and only because the linearization of the chemical source terms is performed according to (55). To achieve further sparsity of the system matrix, in these element matrices off-diagonal entries are neglected. Accordingly and consistently, in the diagonal submatrices of $\boldsymbol{A}_{T,e}$ and hence $\boldsymbol{A}_T$, the off-diagonal contributions resulting from the linearization of the chemical source terms are neglected.

4. Adaptive gridding

4.1. Refinement indicator

In this work we use an a posteriori error indicator to identify in the domain of integration regions where the spatial discretization error is large or small, respectively. The derivation of the indicator is based on two known properties of finite-element solution:

1. As described in the previous section, a finite-element approximation is composed of polynomial functions that are taken piecewise over the elements. Consequently, the numerical solution is not smooth: the normal derivative of a dependent variable jumps across the edge common to two adjacent elements. The size of the jump is taken as a first measure for the local discretization error.
2. As described in Section 2, Green's theorem is used in the derivation of the weak formulation of the governing equations. As a consequence, the residuals of the governing Eqs. (1)–(4), determined on the basis of the finite-element solution, generally are not zero. Their size is taken as a second measure for the local discretization error.

For each of the governing Eqs. (1)–(4), a local a posteriori error indicator has been derived – details of the derivation can be found in [15]. As an example, in the following the energy equation is considered. The indicator $\eta_{e,T}$ on an element Ω_e – with area K_e, edges γ_e, and sidelengths L_{γ_e} – is obtained as

$$\eta_{e,T} = C_1\sqrt{K_e}||R_T^h||_{\Omega_e} + C_2\sum_{\gamma_{e,in}}\sqrt{L_{\gamma_e}}||\lceil\lambda\frac{\partial T_e^h}{\partial n}\rceil||_{\gamma_{e,in}} + C_3\sum_{\gamma_{e,N}}\sqrt{L_{\gamma_e}}||\left(\lambda\nabla T^h\cdot\boldsymbol{n}-q_n\right)||_{\gamma_{e,N}}, \quad e=1,\ldots,E. \tag{68}$$

Here R_T^h denotes the residual of the energy equation as obtained by substituting the finite-element solution; C_1, C_2 and C_3 are empirical constants, and $\|\cdot\|_\Omega$ denotes the L^2-norm,

$$\|g\|_\Omega := \sqrt{\int_\Omega g^2\,\mathrm{d}\Omega}. \tag{69}$$

The second term in (68) describes the jump in the normal derivatives across the inner edge $\gamma_{e,in}$ common to two adjacent elements. The third term takes into account that on Neumann boundaries $\gamma_{e,N}$ the numerical approximation does not necessarily fulfill exactly the boundary condition.

What remains to be specified are the dependent variables on which the adaptive gridding is to be based. For instance, adaptive gridding can be based on one, several, or all dependent variables. Generally, a weighted average of all dependent variables is taken as indicator:

$$\eta_e := \sum_{\text{all } i}\omega_i\eta_{e,i}, \quad \sum_{\text{all } i}\omega_i = 1, \quad i = u,v,p,T,Y_1,\ldots,Y_{N-1}. \tag{70}$$

4.2. Adaptation procedure

The refinement procedure involves the following general steps:

1. Obtain a converged solution on an initial or intermediate triangulation.
2. For each element evaluate the local indicator η_e and the sum

   $$\eta := \sum_{e=1}^{E}\eta_e.$$

   For the purpose of evaluation of the adaptation criteria, instead of any two elements that previously were obtained by a green refinement [33], their father is considered with his indicator taken as the sum of the two.
3. Sort indicators and hence cells according to magnitude such that

   $$\eta_1 \leqslant \eta_2 \leqslant \cdots \leqslant \eta_E.$$

4. Prescribe percentages $\underline{C}$ and $\overline{C}$ and a maximum refinement level N_A. Determine N_C such that $\sum_{e=1}^{N_C}\eta_e \leqslant \underline{C}\eta$ and $\sum_{e=1}^{N_C+1}\eta_e > \underline{C}\eta$, and mark the first N_C elements for subsequent coarsening. Similarly, determine N_R such that $\sum_{e=E-N_R+1}^{E}\eta_e \leqslant \overline{C}\eta$ and $\sum_{E-N_R}^{E}\eta_e > \overline{C}\eta$, and mark the last N_R elements for subsequent refinement.
5. If adaptation is required, apply the rules for mesh refinement and coarsening according to Kornhuber and Roitzsch [33] and Wassenberg [34]. Note that, (i), the refinement rules are applied only to those elements that have not yet reached the maximum refinement level and, (ii), a mesh is not allowed to become coarser than the initial mesh.

6. If the mesh has been adapted, assign interpolated values of the dependent variables to the new grid-points, and restart the integration.

For combustion problems of the non-propagating type [15] (these are not the topic of the present paper and therefore results are not included here) extensive testing of adaptivity and its effect on the solutions was done. In particular, it was ensured that with the chosen parameter values there was no smearing or other falsification of the solutions. Typical numerical values for the parameters are $\underline{C} = 0.01$ and $\overline{C} = 0.5$. A typical maximum refinement level is $N_A = 5$, although in some cases up to 8 refinement levels were used to ensure grid-independent results without artificial thickening of the flame.

5. Solution strategy

Fig. 1 shows a schematic flow diagram of the overall solution procedure. A computation is started with an initial triangulation $\mathscr{T}_0^h$, an initial guess $\mathscr{U}_0^0$ and – if timestepping is required – an initial timestep size Δt^0; typical values for Δt^0 are 10^{-7}–10^{-6} s. Simpler combustion problems of the non-propagating type have been found to work well without timestepping [15], but all the results presented below were obtained with timestepping. For these calculations it was found, that the number of timesteps required to approach a

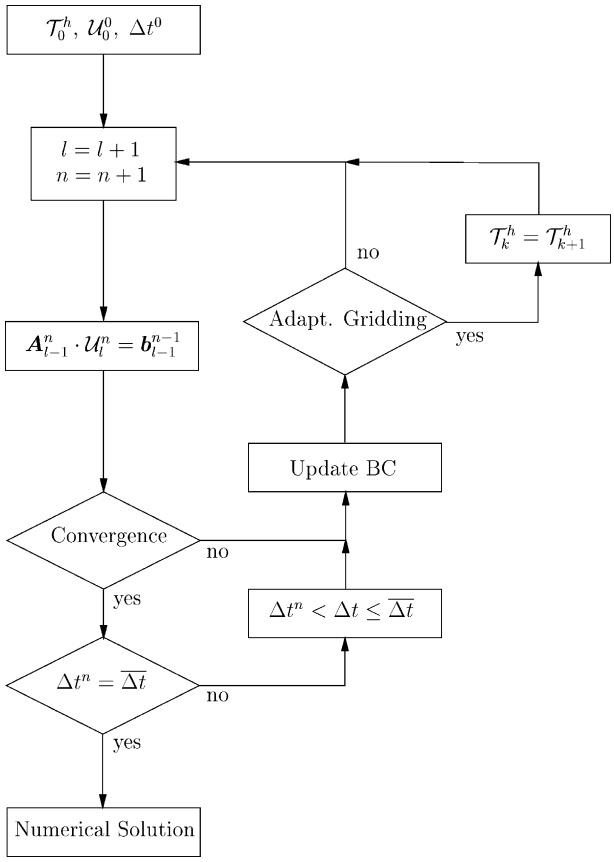

Fig. 1. Schematic flow diagram of the overall solution procedure.

steady solution to a specific overall problem is independent of the work required at each timestep for the solution of the underlying non-linear difference equations. Therefore, the Picard iterations were abandoned. After each timestep, a convergence criterion is evaluated. As long as convergence has not yet been achieved, (i), every N_{bc} timesteps the boundary conditions are updated according to Section 2.4 and, (ii), every N_{ag} timesteps the adaptive-gridding procedure is carried out. For problems with a steady-state solution, the timestep size is gradually increased from its initial value up to an upper bound $\overline{\Delta t}$ to be specified. In general, values of up to $\overline{\Delta t} = 10^{20}$ s are possible. However, for the propagating flames considered in this paper, updating of the speed of the frame of reference, S, and of the boundary conditions was found to require values as small as 10^{-4} s for $\overline{\Delta t}$ combined with values of 3–5 for N_{bc}.

If, with $N_{bc} = 1$, in five successive timesteps convergence has been achieved, the solution is adopted as the solution to the steady-state problem.

6. Example results

The numerical results presented here have been obtained with the models of molecular transport and thermodynamics outlined in Appendix A, and with the reaction mechanisms given in Appendix B.

6.1. Ozone flames

Presented here are results for ozone flames propagating steadily with global speed $S_G := \mid S(\infty) \mid$ in a planar, horizontal channel from right to left into a quiescent fresh mixture; behind a flame, hot combustion products flow to the right. Due to the symmetry of the problem, only the upper half of the channel corresponding to the dashed part in Fig. 2, top, needs to be considered. Three different cases are studied. These cases have in common that the fresh mixture far ahead of the flame contains no atomic oxygen, that the initial ozone mass fraction is 0.25, that the unburnt gas temperature is 300 K and that the channel walls are impermeable to all species. In all cases the plane of symmetry is located at $y' = 0$, the wall at $y' = 2.5$ mm, and the length of the domain of integration is 25 mm although, in most figures, only a portion is shown. It has been ensured that this length is sufficient for the results to be independent of the placement of both the inflow and the outflow boundary.

The cases differ in the wall conditions for velocity and temperature. Specifically, case I assumes no-slip conditions for velocity and an isothermal wall at 300 K, case II no-slip conditions and an adiabatic wall; case III corresponds to an adiabatic wall with slip conditions.

Figs. 2–5 pertain to case I. Here, as a consequence of the cold wall, local flame extinction occurs in the vicinity of the wall leading to a meniscus-like flameshape – subsequently flames of such shape are referred to as *meniscus flames.* Shown in Fig. 2, bottom, are the final mesh and a contour plot of the heat-release rate. The mesh represents three levels of refinement, the number of elements is 5769, the number gridpoints 12,000.

For S_G the value of 0,309 m/s has been obtained which is greater than the value of 0,283 m/s obtained for the laminar flamespeed S_L of the planar, effectively 1D, flame. The difference between S_G and S_L is best explained by reference to Fig. 3 which shows the schematic of a curved flamefront with various velocities in Galilean-transformed space. Specifically, in the figure the thermal-diffusional limit is assumed and the flame is taken as a discontinuity of time-invariant shape. Just ahead of the flame the component of velocity normal to the front is taken to be of constant magnitude S_L; therefore, a variation of the upstream velocity U_S with y is required such that U_S increases from the value S_L at the plane of symmetry towards the wall. Hence, since mass conservation requires S_G to be a suitably defined cross-sectional average of U_S, S_G is greater than $U_S(y = 0) = S_L$.

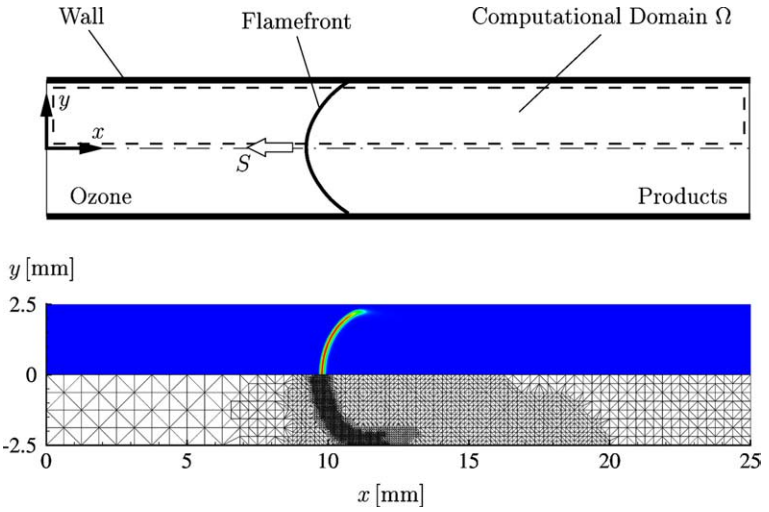

Fig. 2. Ozone flame propagating in a planar channel. Top: Geometry and computational domain. Bottom: Final mesh and contour plot of heat-release rate.

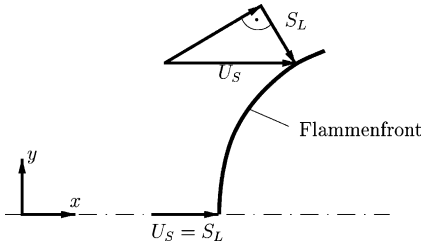

Fig. 3. Schematic representation of a curved flamefront with velocities in Galilean-transformed space.

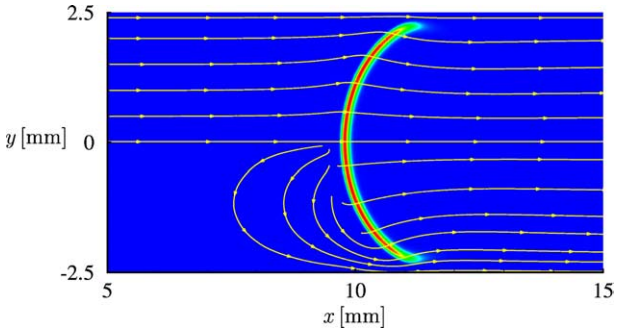

Fig. 4. Streamlines and heat-release rate for the ozone flame of case I. Top: in the Galilean $(\boldsymbol{x}', t)$ coordinate system. Bottom: in the laboratory $(\boldsymbol{x}, t)$ coordinate system.

The effect of $S_G > S_L$ on the flowfield can be seen from Fig. 4. In the top of the figure, streamlines are plotted in the Galilean-transformed space, in the bottom streamlines in physical space. In the vicinity of the symmetry plane, the Galilean streamlines show the divergence and convergence ahead and behind the

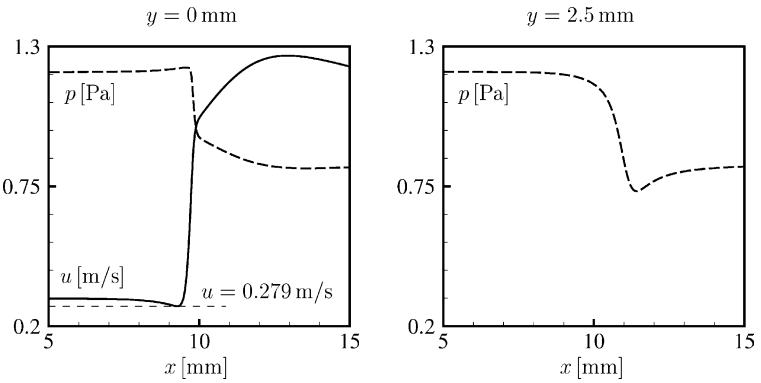

Fig. 5. Pressure and longitudinal component of velocity as a function of x' at the plane of symmetry (left) and at the wall (right) and for case I.

flame, respectively, which is typical and well-known for flames with convex curvature; closer to the cold wall, the streamlines are disturbed due to local flame quenching. The streamlines in physical space show that, due to expansion, the flame pushes the fresh gases ahead of it, with a slip-through in the vicinity of the wall; again, the latter is the result of local flame quenching at the cold wall.

The observed self-induced flow upstream of the flame has been termed "squish-flow" [19]. Its physical origin can be discussed by reference to Fig. 5. There, on the left, pressure p and longitudinal velocity component u are plotted vs. x on the axis of symmetry; on the right, p along the wall is plotted (recall: $u = v = 0$ there). It can be seen, that on the axis the flow is decelerating from $S_G > S_L$ to approximately S_L, which is accompanied by an accordingly weak pressure rise. Through the flame the usual strong pressure drop and strong acceleration are observed. At the wall, the pressure drops continuously to a local minimum behind the flame, which is consistent with a continuous acceleration of the flow close to the wall. The mild pressure increase behind the flame is the result of the continuously accumulating convective heat loss through the walls.

Figs. 6 and 7 pertain to case II: adiabatic walls but still no-slip conditions for velocity. In contrast to the cold wall of case I, no heat losses occur to the wall; hence in the vicinity of the wall, no flame quenching occurs and, as a consequence, a flame of tulip shape, termed "tulip flame" [19], results. The tulip flame and the meniscus flame have in common that $S_G > S_L$. However, in this example, the tulip flame propagates faster ($S_G = 0.375$ m/s) than the meniscus flame ($S_G = 0.309$ m/s). For the tulip flame, the squish-flow ahead of the flame is is directed towards the axis of symmetry. The reason for the change in direction is the gas

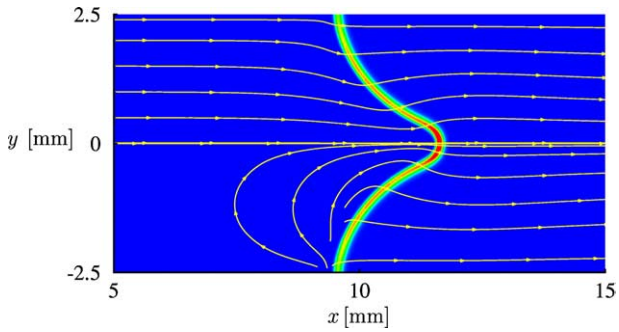

Fig. 6. As Fig. 4 but for case II.

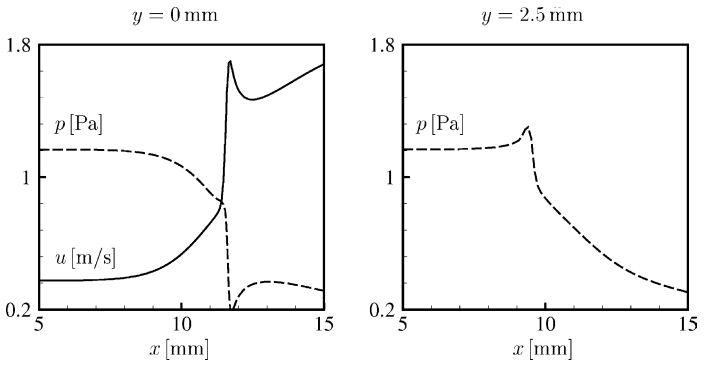

Fig. 7. As Fig. 5 but for case II.

expansion near the wall. Because of the no-slip condition for velocity, expansion there does not result in acceleration but in pressure rise. A pressure gradient towards the symmetry plane results, which induces the observed direction of slip flow. The difference between the maximum pressure p_{max} (at the wall) and the pressure in the undisturbed fresh mixture far ahead of the flame is found to be approximately 10 times larger than for the meniscus flame of case I where p_{max} occurred on the axis.

To demonstrate the influence of the no-slip condition for velocity, we now consider case III corresponding to adiabatic walls and slip conditions for velocity. Shown in Fig. 8, top and bottom, are, in the familiar presentation of above, results for two flames, viz., streamlines and heat-release rate. Both flames have been obtained for identical boundary conditions, but the initial conditions were different: for the meniscus flame in the top picture, initially a convex flame shape was assumed, for the tulip flame in the

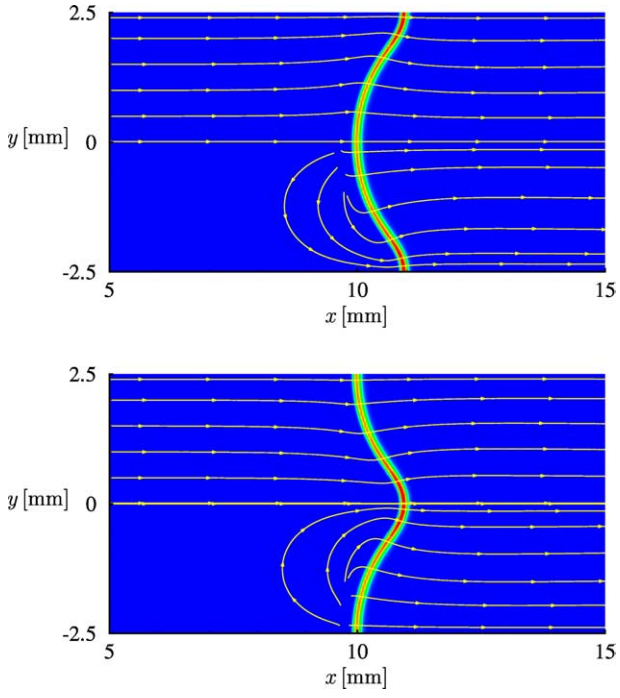

Fig. 8. As Fig. 4 but for case III.

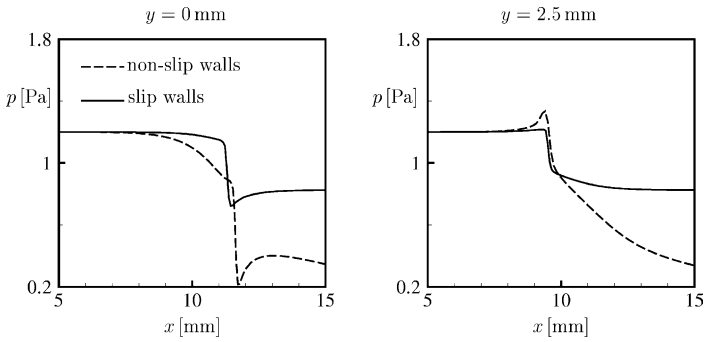

Fig. 9. The influence of no-slip and slip wall condition on the adiabatic flame: pressure as a function of x' at the plane of symmetry (left) and at the wall (right).

bottom picture, a concave shape. Thus, these results illustrate that for the boundary conditions of case III the solution is not unique but depends on the initial conditions. Similar observations were made earlier [19], though in these investigations a different geometry and simpler physical and numerical models were employed. It is important to note that for case III the boundary conditions at the symmetry plane and the wall are formally identical. As a consequence, the wall can be viewed as another plane of symmetry and hence each of the two flame shapes shown in Fig. 8 can be interpreted as representing one amplitude of a flame of 2D periodic shape and infinite extent. The results shown here represent the 2D counterpart of the hydrodynamic instability discovered by Darrieus and Landau which plays an important role in the explanation of cellular flames [21]. The global flame speed S_G is $0,307$ m/s.

To investigate the influence of the velocity boundary condition, it suggests itself to compare the meniscus flames of Figs. 8(top) and 4 and the tulip flames of Figs. 8(bottom) and 7, respectively. To this end, in the following attention is focused on the tulip flame. Shown in Fig. 9 are the profiles of pressure in the form familiar from cases II and III. From the right picture it is seen that, as it is to be expected on physical grounds, for slip conditions the local maximum of pressure at the wall nearly vanishes. As a consequence, in comparison to the case with slip conditions, a substantially weaker squish flow to the axis results which in turn implies the observed weaker curvature of the tulip flame. In particular, the local pressure excess at the wall is so small that, in view of hydrodynamic instability, the location of maximum pressure may shift to the axis, thereby inducing squish flow to the outside and bringing about the meniscus flame.

6.2. Hydrogen–oxygen flames

Various hydrogen–air flames have been computed, all with no-slip conditions at the wall. Two cases of temperature boundary conditions have been distinguished, viz. (i) constant wall temperature T_W and (ii) adiabatic wall. For both cases computations with various values of the equivalence ratio were performed. The computed flames are summarized in Table 2, where also S_L is given.

As for the ozone flame, for adiabatic walls tulip flame shapes are predicted. However, in contrast to the ozone flame, for constant wall temperature flame shapes are obtained that exhibit both tulip and meniscus flame features.

In the following, first the tulip flames are discussed.

Shown in Fig. 10 is a sequence of flameshapes (again in terms of the heat-release rate) and flowfields for, from top to bottom, $\phi = 0.5, 1, 2.5$ and 5. It is seen that for the lowest value of ϕ the flame tip is open. Responsible for the tip opening are (i) the local diffusive loss towards the flame front of H_2 and H such that locally the equivalence ratio falls below the lean flammability limit and (ii) local flame extinction due to

Table 2
Summary of computed hydrogen–air flames

ϕ	0.5	1	2.5	5
S_L (m/s)	0.39	2.35	2.74	1076
S_G (m/s) (constant T_W)	0.77	2.88	3.03	1085
S_G (m/s) (adiabatic wall)	1.39	4.16	3.95	1080

excessive flame curvature. It is seen that with increasing ϕ both the ratio S_G/S_L and the tip curvature decrease consistently to each other, cf. the above section on the ozone flame. Shown in Fig. 11 are contour plots for the stoichiometric hydrogen–air flame of Fig. 10 for, from top to bottom, the temperature and the mass fractions of H, OH, O and H_2O_2. These results are as to be expected on physical grounds and clearly demonstrate the capability of the numerical approach to capture even sensible details of complex flame structures.

Similar as in Fig. 10, shown in Fig. 12 is a sequence of flameshapes and flowfields, but now for a constant wall temperature of 300 K. Again, from top to bottom, the pictures pertain to $\phi = 0.5$, 1, 2.5 and 5, respectively. It is seen that for the lean to moderately rich mixtures flame structures are predicted that consist of two meniscus-like flames in which, in the vicinity of the plane of symmetry, a tulip flame is embedded.

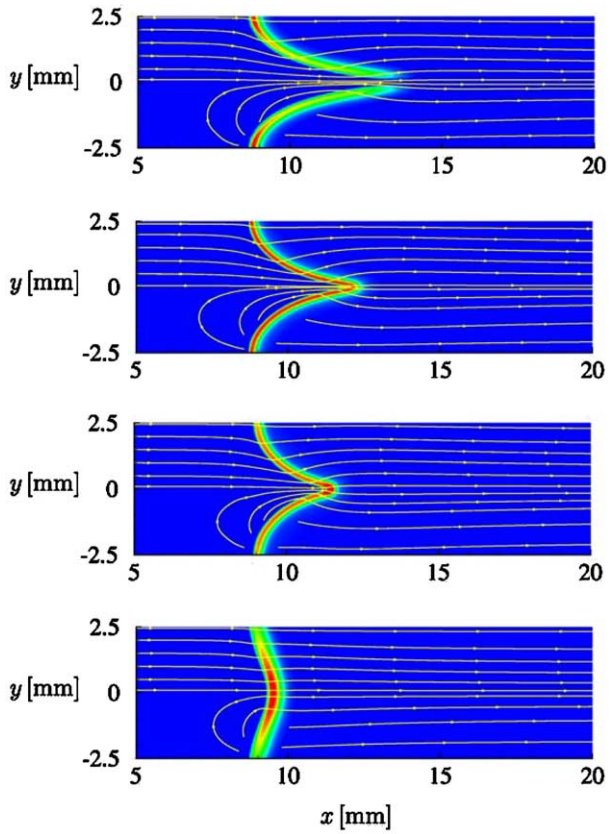

Fig. 10. Streamlines and heat-release rate for hydrogen–air flames subject to no-slip and adiabatic-wall boundary conditions for, from top to bottom, $\phi = 0.5, 1, 2.5$ and 5. Mode of presentation as in Fig. 4.

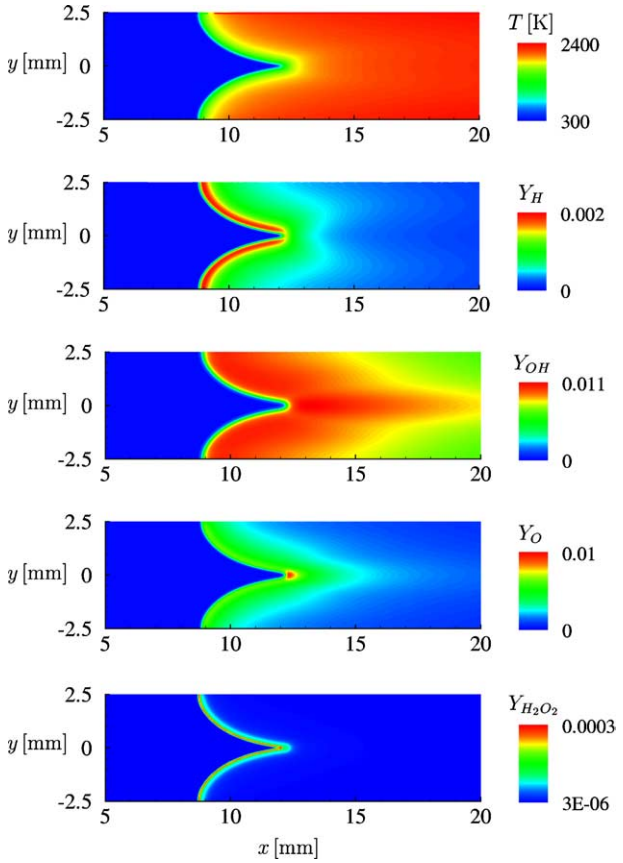

Fig. 11. Contour plots for the stoichiometric hydrogen–air flame of Fig. 10 for, from top to bottom, the temperature and the mass fractions of H, OH, O and H_2O_2.

Only for the very rich mixtures pure meniscus flames are established. The leanest of the four flames has an open flame tip for the reasons already discussed above.

7. Summary

This paper presents a finite element formulation for the simulation of laminar, chemically reactive flows in the low Mach number regime. The formulation is based on the governing equations of mass, species mass, momentum and energy.

Stabilization terms leading to streamline upwinding are introduced into the governing equations in order to avoid numerical instabilities in convection-dominated regions of the flow. These terms are quantified according to the local and instantaneous magnitude of the relevant characteristic non-dimensional parameters.

Discretization of the variational formulation of the governing equations is carried out using the standard Galerkin Method employing triangular Taylor–Hood elements. Linearization of the chemical source terms is achieved by Newton-iterations, linearization of the remaining non-linear terms by Picard-iterations. The discretization with respect to time is expressed in terms of backward Euler differences. An exception is the

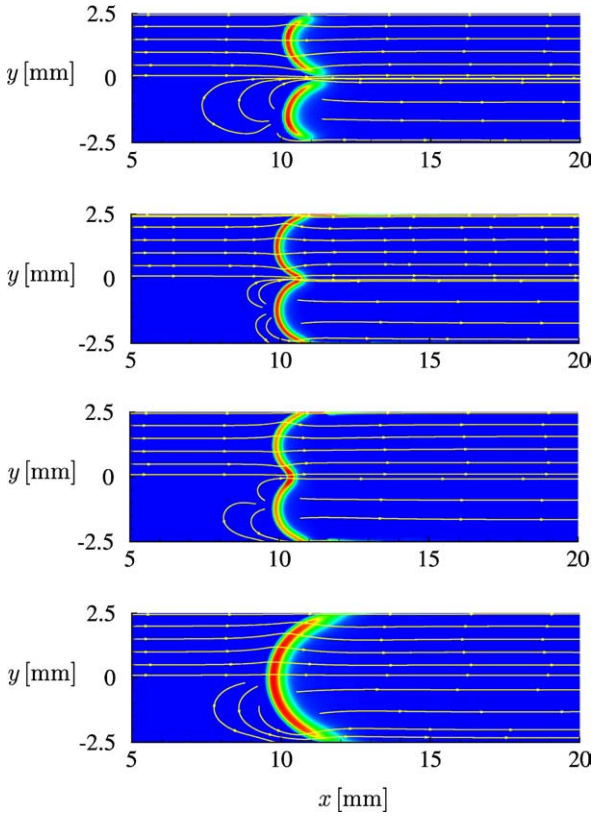

Fig. 12. As Fig. 10, but for constant wall temperature of 300 K.

continuity equation, where the introduction of a perturbation term leads to significantly shorter computing times.

In the linearized discrete formulation, the continuity equations and the momentum equations are decoupled from the energy and species conservation equations. Hence, at each time or iteration step, rather than solving one large linear system of equations two smaller systems are solved in succession.

The simulations are carried out on unstructured grids that are subjected to local refinement and adaptation. The self-adaptivity of the grid is controlled by a posteriori residual error indicator.

The considered steadily propagating laminar ozone decomposition and diluted hydrogen/oxygen flames in flat channels could be handled efficiently with a Galilei transformation. Numerical results for such flames with different boundary conditions at the wall and varying equivalence ratios are presented. Flames with meniscus-like and tulip-like flameshapes were found. The significant differences in these flameshapes are discussed in detail.

Appendix A. Transport and thermodynamic model

Following [35] it is assumed that the diffusion velocity $\boldsymbol{V}_i$, $i = 1, \ldots, N$, is composed of three parts, i.e.,

$$\boldsymbol{V}_i = \boldsymbol{V}_i^D + \boldsymbol{V}_i^{\mathrm{T}} + \boldsymbol{V}_{\mathrm{c}}. \tag{A.1}$$

Here $\boldsymbol{V}_i^D$ is the ordinary-diffusion velocity for which an approximation recommended by Hirschfelder and Curtiss [36,37],

$$\boldsymbol{V}_i^D = -\frac{D_i}{X_i}\nabla X_i, \quad i = 1, \ldots, N \tag{A.2}$$

is adopted; here X_i denotes the mole fraction of species i and D_i is its mixture-averaged diffusion coefficient which is given explicitly in terms of the binary diffusion coefficients D_{ij} by

$$D_i = \frac{1 - Y_i}{\sum_{\substack{j=1 \\ j\neq i}}^{N} X_j / D_{ij}}. \tag{A.3}$$

In Eq. (A.1), $\boldsymbol{V}_i^{\mathrm{T}}$ is the thermal diffusion velocity,

$$\boldsymbol{V}_i^{\mathrm{T}} = -\frac{D_i^{\mathrm{T}}}{\rho Y_i T}\nabla T, \quad i = 1, \ldots, N, \tag{A.4}$$

a non-zero value of which is included only for the light species H and H_2. In Eq. (A.4) T is the temperature and D_i^{T} is the thermal-diffusion coefficient of species i which is evaluated following [37,38]. The correction velocity $\boldsymbol{V}_{\mathrm{c}}$ appearing in Eq. (A.1) is determined according to [35,39].

The dynamic viscosity and the thermal conductivity of the mixture are calculated from the respective properties of the pure species according to

$$\mu = \frac{1}{2}\left(\sum_{i=1}^{N} X_i \mu_i + \left[\sum_{i=1}^{N} \frac{X_i}{\mu_i}\right]^{-1}\right) \tag{A.5}$$

and

$$\lambda = \frac{1}{2}\left(\sum_{i=1}^{N} X_i \lambda_i + \left[\sum_{i=1}^{N} \frac{X_i}{\lambda_i}\right]^{-1}\right). \tag{A.6}$$

For details of the evaluation of the species transport coefficients and of the species thermodynamic properties reference is given to [37,38].

Appendix B. Reaction mechanisms

The following reaction mechanisms are used for the computations in this work (see Tables 3 and 4).

Table 3
Reaction mechanism used for the ozone flames

No.	Reaction	A (mol, cm, s)	n	E (kJ/mol)
1	$O_3 + M' \rightarrow O_2 + O + M'$	4.310E + 14	0.00	92.79
2	$O_2 + O + M' \rightarrow O_3 + M'$	1.745E + 13	0.00	−4.12
3	$O_3 + O \rightarrow 2O_2$	1.140E + 13	0.00	19.12
4	$2O_2 \rightarrow O_3 + O$	1.042E + 13	0.00	417.79
5	$2O + M' \rightarrow O_2 + M'$	1.380E + 18	−1.00	1.42
6	$O_2 + M' \rightarrow 2O + M'$	3.116E + 19	−1.00	496.99

Table 4
Reaction mechanism used for the hydrogen/air flames

No.	Reaction	A (mol, cm, s)	n	E (kJ/mol)
1	$O_2 + H \rightarrow OH + O$	2.000E + 14	0.00	70.30
2	$OH + O \rightarrow O_2 + H$	1.568E + 13	0.00	3.52
3	$H_2 + O \rightarrow OH + H$	5.060E + 04	2.67	26.30
4	$OH + H \rightarrow H_2 + O$	2.222E + 04	2.67	18.29
5	$H_2 + OH \rightarrow H_2O + H$	1.000E + 08	1.60	13.80
6	$H_2O + H \rightarrow H_2 + OH$	4.312E + 08	1.60	76.46
7	$OH + OH \rightarrow H_2O + O$	1.500E + 09	1.14	0.42
8	$H_2O + O \rightarrow OH + OH$	1.473E + 10	1.14	71.09
9	$O_2 + H + M' \rightarrow HO_2 + M'$	2.300E + 18	−0.80	0.00
10	$HO_2 + M' \rightarrow O_2 + H + M'$	3.190E + 18	−0.80	195.39
11	$HO_2 + H \rightarrow OH + OH$	1.500E + 14	0.00	4.20
12	$HO2 + H \rightarrow H_2 + O_2$	2.500E + 13	0.00	2.90
13	$HO_2 + OH \rightarrow H_2O + O_2$	6.000E + 13	0.00	0.00
14	$HO_2 + H \rightarrow H_2O + O$	3.000E + 13	0.00	7.20
15	$HO_2 + O \rightarrow OH + O_2$	1.800E + 13	0.00	−1.70
16	$HO_2 + HO_2 \rightarrow H_2O_2 + O_2$	2.500E + 11	0.00	−5.20
17	$OH + OH + M' \rightarrow H_2O_2 + M'$	3.250E + 22	−2.00	0.00
18	$H_2O_2 + M' \rightarrow OH + OH + M'$	1.692E + 24	−2.00	202.29
19	$H_2O_2 + H \rightarrow H_2O + OH$	1.000E + 13	0.00	15.00
20	$H_2O_2 + OH \rightarrow H_2O + HO_2$	5.400E + 12	0.00	4.20
21	$H_2O + HO_2 \rightarrow H_2O_2 + OH$	1.802E + 13	0.00	134.75
22	$H + H + M' \rightarrow H_2 + M'$	1.800E + 18	−1.00	0.00
23	$OH + H + M' \rightarrow H_2O + M'$	2.200E + 22	−2.00	0.00
24	$O + O + M' \rightarrow O_2 + M'$	2.900E + 17	−1.00	0.00

Appendix C. Weak formulation of the governing equations for the 2D planar and axisymmetric case

In the following equations $c = 0$ indicates the planar and $c = 1$ the axisymmetric case.

C.1. Continuity equation

$$\int_\Omega \psi \left[\frac{\partial u}{\partial x} + \frac{1}{y^c} \frac{\partial (v y^c)}{\partial y} \right] y^c \, \mathrm{d}\boldsymbol{x} + - \int_\Omega \ln \rho \left[\frac{\partial (\psi u)}{\partial x} + \frac{1}{y^c} \frac{\partial (\psi v y^c)}{\partial y} \right] y^c \, \mathrm{d}\boldsymbol{x}$$
$$= - \int_\Gamma \psi \ln \rho (\boldsymbol{v} \cdot \boldsymbol{n}) y^c \, \mathrm{d}s \quad \forall \psi \in H^1(\Omega), \tag{C.1}$$

with

$$- \int_\Gamma \psi \ln \rho (\boldsymbol{v} \cdot \boldsymbol{n}) y^c \, \mathrm{d}s = - \int_\Gamma \psi (\ln \rho) u y^c \, \mathrm{d}y + \int_\Gamma \psi (\ln \rho) v y^c \, \mathrm{d}x. \tag{C.2}$$

C.2. Momentum equation in $\boldsymbol{x}$-direction

$$\int_\Omega \phi \rho \left(u \frac{\partial u}{\partial x} + v \frac{\partial u}{\partial y} \right) y^c \, \mathrm{d}\boldsymbol{x} - \int_\Omega p_\mathrm{m} \frac{\partial \phi}{\partial x} y^c \, \mathrm{d}\boldsymbol{x} + \int_\Omega \mu \left[2 \frac{\partial u}{\partial x} \frac{\partial \phi}{\partial x} + \left(\frac{\partial u}{\partial y} + \frac{\partial v}{\partial x} \right) \frac{\partial \phi}{\partial y} \right] y^c \, \mathrm{d}\boldsymbol{x}$$
$$- \int_\Omega \phi \rho g_1 y^c \, \mathrm{d}\boldsymbol{x} = \int_\Gamma \phi s_x y^c \, \mathrm{d}s \quad \forall \phi \in V^1(\Omega). \tag{C.3}$$

To evaluate the boundary integral on the r.h.s., two alternatives are available. viz., alternative 1:

$$\begin{aligned}\int_\Gamma \phi s_x y^c \,\mathrm{d}s &= \int_\Gamma \phi(s_n \boldsymbol{n} + s_\tau \boldsymbol{\tau})\boldsymbol{i} y^c \,\mathrm{d}s = \int_\Gamma \phi(s_n n_1 + s_\tau \tau_1) y^c \,\mathrm{d}s = \int_\Gamma \phi s_n y^c \,\mathrm{d}y + \int_\Gamma \phi s_\tau y^c \,\mathrm{d}x \\ &= \int_\Gamma \phi\left[-p_\mathrm{m} + 2\mu\frac{\partial v_n}{\partial n}\right] y^c \,\mathrm{d}y + \int_\Gamma \phi\mu\left[\frac{\partial v_\tau}{\partial n} + \frac{\partial v_n}{\partial \tau}\right] y^c \,\mathrm{d}x \end{aligned} \tag{C.4}$$

and alternative 2:

$$\begin{aligned}\int_\Gamma \phi s_x y^c \mathrm{d}s &= \int_\Gamma \phi(\boldsymbol{s}\cdot\boldsymbol{i}) y^c \,\mathrm{d}s = \int_\Gamma \phi\left[p_\mathrm{m}\boldsymbol{n} + \mu\left(\frac{\partial \boldsymbol{v}}{\partial n} + \nabla u_n\right)\right]\cdot \boldsymbol{i} y^c \,\mathrm{d}s \\ &= \int_\Gamma \phi\left[p_\mathrm{m} n_1 + \mu\left(\nabla u\cdot\boldsymbol{n} + \frac{\partial(\boldsymbol{v}\cdot\boldsymbol{n})}{\partial x}\right)\right] y^c \,\mathrm{d}s \\ &= \int_\Gamma \phi\left[p_\mathrm{m} n_1 + \mu\left(\frac{\partial u}{\partial n} + \frac{\partial u}{\partial x} n_1 + \frac{\partial v}{\partial x} n_2\right)\right] y^c \mathrm{d}s \\ &= \int_\Gamma -\phi p_\mathrm{m} y^c \,\mathrm{d}y + \left[\int_\Gamma \phi\mu\frac{\partial u}{\partial n} y^c \,\mathrm{d}s + \int_\Gamma \phi\mu\frac{\partial u}{\partial x} y^c \,\mathrm{d}y - \int_\Gamma \phi\mu\frac{\partial v}{\partial x} y^c \,\mathrm{d}x\right]. \end{aligned} \tag{C.5}$$

C.3. Momentum equation in **y**-direction

$$\begin{aligned}&\int_\Omega \phi\rho\left(u\frac{\partial v}{\partial x} + v\frac{\partial v}{\partial y}\right) y^c \,\mathrm{d}\boldsymbol{x} - \int_\Omega p_\mathrm{m}\frac{\partial \phi}{\partial y}\,\mathrm{d}\boldsymbol{x} + \int_\Omega \mu\left[\left(\frac{\partial u}{\partial y} + \frac{\partial v}{\partial x}\right)\frac{\partial \phi}{\partial x} + 2\frac{\partial v}{\partial y}\frac{\partial \phi}{\partial y}\right] y^c \,\mathrm{d}\boldsymbol{x} \\ &\quad + c\int_\Omega 2\mu\frac{v\phi}{y}\,\mathrm{d}\boldsymbol{x} - \int_\Omega \phi\rho g_2 y^c \,\mathrm{d}\boldsymbol{x} = \int_\Gamma \phi s_y y^c \,\mathrm{d}s \quad \forall \phi \in V^1(\Omega). \end{aligned} \tag{C.6}$$

To evaluate the boundary integral on the r.h.s., two alternatives are available. viz., alternative 1:

$$\begin{aligned}\int_\Gamma \phi s_y y^c \,\mathrm{d}s &= -\int_\Gamma \phi s_n y^c \,\mathrm{d}x + \int_\Gamma \phi s_\tau y^c \,\mathrm{d}y \\ &= -\int_\Gamma \phi\left[-p_\mathrm{m} + 2\mu\frac{\partial v_n}{\partial n}\right] y^c \,\mathrm{d}x + \int_\Gamma \phi\mu\left[\frac{\partial v_\tau}{\partial n} + \frac{\partial v_n}{\partial \tau}\right] y^c \,\mathrm{d}y. \end{aligned} \tag{C.7}$$

and alternative 2:

$$\begin{aligned}\int_\Gamma \phi s_y y^c \mathrm{d}s &= \int_\Gamma \phi(\boldsymbol{s}\cdot\boldsymbol{j}) y^c \mathrm{d}s = \int_\Gamma \phi\left[p_\mathrm{m} n_2 + \mu\left(\nabla v\cdot\boldsymbol{n} + \frac{\partial(\boldsymbol{v}\cdot\boldsymbol{n})}{\partial y}\right)\right] y^c \mathrm{d}s \\ &= \int_\Gamma \phi p_\mathrm{m} y^c \,\mathrm{d}x + \left[\int_\Gamma \phi\mu\frac{\partial v}{\partial n} y^c \,\mathrm{d}s + \int_\Gamma \phi\mu\frac{\partial u}{\partial y} y^c \,\mathrm{d}y - \int_\Gamma \phi\mu\frac{\partial v}{\partial y} y^c \,\mathrm{d}x\right]. \end{aligned} \tag{C.8}$$

C.4. Energy equation

$$\begin{aligned}&\int_\Omega \phi c_p\rho\left(u\frac{\partial T}{\partial x} + v\frac{\partial T}{\partial y}\right) y^c \,\mathrm{d}\boldsymbol{x} + \int_\Omega \lambda\left(\frac{\partial T}{\partial x}\frac{\partial \phi}{\partial x} + \frac{\partial T}{\partial y}\frac{\partial \phi}{\partial y}\right) y^c \,\mathrm{d}\boldsymbol{x} \\ &\quad - \int_\Omega \phi\left(\frac{\partial T}{\partial x}\sum_{i=1}^{N} c_{p,i}\rho D_i\frac{\partial Y_i}{\partial x} + \frac{\partial T}{\partial y}\sum_{i=1}^{N} c_{p,i}\rho D_i\frac{\partial Y_i}{\partial y}\right) y^c \,\mathrm{d}\boldsymbol{x} - \int_\Omega \phi w_T y^c \,\mathrm{d}\boldsymbol{x} \\ &\quad = \int_\Gamma \phi\lambda\frac{\partial T}{\partial n} y^c \,\mathrm{d}s \quad \forall \phi \in V^1(\Omega). \end{aligned} \tag{C.9}$$

C.5. Species equations

$$\int_\Omega \phi\rho\left(u\frac{\partial Y_i}{\partial x}+v\frac{\partial Y_i}{\partial y}\right)y^c\,\mathrm{d}\boldsymbol{x}+\int_\Omega \phi\rho D_i\left(\frac{\partial Y_i}{\partial x}\frac{\partial \phi}{\partial x}+\frac{\partial Y_i}{\partial y}\frac{\partial \phi}{\partial y}\right)y^c\,\mathrm{d}\boldsymbol{x}-\int_\Omega \phi w_{Y_i}y^c\,\mathrm{d}\boldsymbol{x}$$
$$=\int_\Gamma \phi\rho D_i\frac{\partial Y_i}{\partial n}\,\mathrm{d}s,\quad i=1,\ldots,N\quad \forall\phi\in V^1(\Omega). \tag{C.10}$$

Appendix D. Derivation of Eqs. (58)–(60)

For

$$K_{ij}:=\frac{\partial w_i}{\partial Y_j} \tag{D.1}$$

application of the chain-rule yields

$$K_{ij}=\sum_k \frac{\partial w_i}{\partial C_k}\frac{\partial C_k}{\partial Y_j}=\sum_k \frac{\partial w_i}{\partial C_k}\frac{\partial}{\partial Y_j}\left(\frac{\rho Y_k}{W_k}\right)=\sum_k \frac{\partial w_i}{\partial C_k}\left[\frac{\rho}{W_k}\frac{\partial Y_k}{\partial Y_j}+\frac{Y_k}{W_k}\frac{\partial \rho}{\partial Y_j}\right].$$

Since

$$\frac{\partial \rho}{\partial Y_j}=\frac{\partial}{\partial Y_j}\left[\frac{p}{R^0T}\left(\sum_i \frac{Y_i}{W_i}\right)^{-1}\right]=\frac{p}{R^0T}\frac{\partial}{\partial Y_j}\left(\sum_i \frac{Y_i}{W_i}\right)^{-1}=-\frac{\rho}{W_j}\left(\sum_i \frac{Y_i}{W_i}\right)^{-1}=-\rho\overline{W}/W_j,$$

we obtain

$$K_{ij}=\sum_k \frac{\partial w_i}{\partial C_k}\left[\frac{\rho\delta_{jk}}{W_k}-\frac{\rho\overline{W}Y_k}{W_jW_k}\right]=\frac{\rho}{W_j}\left[\frac{\partial w_i}{\partial C_j}-\sum_k \frac{\partial W_i}{\partial C_k}\left(\frac{\overline{W}Y_k}{W_k}\right)\right],$$

i.e.

$$K_{ij}=\frac{\rho}{W_j}\left[\frac{\partial w_i}{\partial C_j}-\sum_k X_k\frac{\partial w_i}{\partial C_k}\right]. \tag{D.2}$$

In the following, three alternatives approximations to the matrix K_{ij} are presented, the first two alternatives being based on (D.2), the third on (D.1). The alternatives are:

(i) Neglecting in (D.2) the sum $\sum_k X_k(\partial w_i/\partial C_k)$; this corresponds to taking $\rho=\text{const}$ for the purpose of evaluating $\partial w_i/\partial Y_j$. Thus

$$K_{ij}\approx\frac{\rho}{W_j}\frac{\partial w_i}{\partial C_j}. \tag{D.3}$$

(ii) Neglecting in (D.2) the sum $\sum_{k\neq j} X_k(\partial w_i/\partial C_k)$. Thus

$$K_{ij} \approx \frac{\rho(1-X_j)}{W_j}\,\frac{\partial w_j}{\partial C_j}. \tag{D.4}$$

(iii) Defining $m_{ij} = 0$ for $(\partial w_i/\partial C_j) = 0$ and $m_{ij} = 1$ otherwise, and taking

$$K_{ij} \approx m_{ij}(\partial w_i/\partial Y_j) \tag{D.5}$$

rather than (D.1).

References

[1] M.D. Smooke, A.A. Turnbull, R.E. Mitchell, D.E. Keyes, Solution of two-dimensional axisymmetric laminar diffusion flames by adaptive boundary value methods, in: C.-M. Brauner, C. Schmidt-Lainé (Eds.), Mathematical Modeling in Combustion and Related Topics, Martinus Nijhoff Publishers, 1988, pp. 261–300.

[2] M.D. Smooke, R.E. Mitchell, D.E. Keyes, Numerical solution of two-dimensional axisymmetric laminar diffusion flames, Combust. Sci. Technol. 67 (1989) 85–122.

[3] Y. Xu, M.D. Smooke, P. Lin, M.B. Long, Primitive variable modeling of multidimensional laminar flames, Combust. Sci. Technol. 90 (1993) 289–313.

[4] U. Maas, J. Warnatz, Detailed numerical simulation of H_2–O_2 ignition in two-dimensional geometries, in: A.L. Kuhl, J.-C. Leyer, A.A. Borisov, W.A. Sirignano (Eds.), Dynamics of Gaseous Combustion, Progress in Astronautics and Aeronautics, vol. 151, AIAA, Washington, DC, 1993, pp. 39–58.

[5] A. Ern, C.C. Douglas, M.D. Smooke, Detailed chemistry modeling of laminar diffusion flames on parallel computers, Int. J. Supercomput. Appl. 9 (1995) 167–186.

[6] B.A.V. Bennett, M.D. Smooke, Local rectangular refinement with application to axisymmetric laminar flames, Combust. Theory Model. 2 (1998) 221–258.

[7] U. Riedel, A finite volume scheme on unstructured grids for stiff chemically reacting flows, Combust. Sci. Technol. 135 (1998) 99–116.

[8] H.C. de Lange, L.P.H. de Goey, Numerical flow modeling in a locally refined grid, Int. J. Numer. Methods Eng. 37 (1994) 497–515.

[9] R.M.M. Mallens, H.C. de Lange, C.H.J. van de Ven, L.P.H. de Goey, Modeling of confined and unconfined laminar premixed flames on slit and tube burners, Combust. Sci. Technol. 107 (1995) 387–401.

[10] L.T. Somers, L.P.H. de Goey, A numerical study of a premixed flame on a slit burner, Combust. Sci. Technol. 108 (1995) 121–132.

[11] A. Ern, V. Giovangigli, Thermal diffusion effects in hydrogen–air and methane–air flames, Combust. Theory Model. 2 (1998) 349–372.

[12] T. Echekki, J.H. Chen, Structure and propagation of methanol-air triple flames, Combust. Flame 114 (1998) 231–245.

[13] P.N. Kioni, K.N.C. Bray, D.A. Greenhalgh, B. Rogg, Experimental and numerical studies of a triple flame, Combust. Flame 116 (1999) 192–206.

[14] R. Becker, M. Braack, R. Rannacher, Numerical simulation of laminar flames at low Mach number by adaptive finite elements, Combust. Theory Model. 3 (1999) 503–534.

[15] B. Michaelis, Simulation zweidimensionaler laminarer Flammen mit der Methode der finiten Elemente, PhD Thesis, Ruhr-Universität Bochum, Germany, 2002.

[16] M. Thiele, J. Warnatz, U. Maas, Geometric study of spark ignition in two dimensions, Combust. Theory Model. 4 (2000) 413–434.

[17] R. Starke, P. Roth, An experimental investigation of flames behavior during cylindrical vessel explosions, Combust. Flame 66 (1986) 249–259.

[18] D. Dunn-Rankin, P.K. Barr, R.F. Sawyer, Numerical and experimental study of tulip flame formation in a closed vessel, in: 21st Symposium (Int.) on Combustion, The Combustion Institute, 1986, pp. 1291–1301.

[19] M. Gonzales, R. Borghi, A. Saouab, Interaction of a flame front with its self-generated flow in an enclosure: the tulip flame phenomenon, Combust. Flame 88 (1992) 201–220.

[20] M. Hishida, S.S. Wirawan, M. Wataru, Comparison between the full chemistry and global reaction models for tulip flame simulation, Trans. Jpn. Soc. Aero. Space Sci. 41 (1999) 209–215.

[21] F.A. Williams, Combustion Theory, second ed., Benjamin/Cummings, Menlo Park, 1985.

[22] K.K. Kuo, Principles of Combustion, Wiley, New York, 1986.

[23] R.G. Rehm, H.R. Baum, The equations of motion for thermally driven, buoyant flows, NBS J. Res. 83 (1978) 297–308.

[24] A. Majda, Compressible Fluid Flow and Systems of Conservation Laws in Several Space Variables, Springer, New York, 1984.
[25] A. Majda, J. Sethian, The derivation and numerical solution of the equations for zero Mach number combustion, Combust. Sci. Technol. 42 (1985) 185–205.
[26] K.B. McGrattan, R.G. Rehm, H.R. Baum, Fire-driven flows in enclosures, J. Comput. Phys. 110 (1994) 285–291.
[27] Th.v. Kármán, Fundamental Equations in Aerothermochemistry, Selected Combustion Problems, Part 2, Butterworths Scientific Publications, London, 1956, pp. 167–184.
[28] P.M. Gresho, Incompressible fluid dynamics: Some fundamental formulation issues, Annu. Rev. Fluid Mech. 23 (1991) 413–453.
[29] C. Cuvelier, A. Segal, A.A. van Steenhoven, Finite Element Methods and Navier–Stokes Equations, D. Reidel Publishing, Dordrecht, 1986.
[30] D.W. Kelly, S. Nakazawa, O.C. Zienkiewicz, J.C. Heinrich, A note on upwinding and anisotropic balancing dissipation in finite element approximations to convective diffusion problems, Int. J. Numer. Methods Eng. 15 (1980) 1705–1711.
[31] R. Peyret, Th.D. Taylor, Computational Methods for Fluid Flow, Springer, New York, 1983.
[32] A.N. Brooks, J.R. Hughes, Streamline upwind Petrov–Galerkin formulations for convection dominated flows with particular emphasis on the Navier–Stokes equations, Comp. Methods Appl. Mech. Eng. 32 (1982) 199–259.
[33] R. Kornhuber, R. Roitzsch, On adaptive grid refinement in the presence of internal or boundary layers, Impact Comp. Sci. Eng. 2 (1990) 40–72.
[34] H. Wassenberg, Entwicklung eines Finite Elemente Rechenprogramms mit selbstadaptivem, mitbewegtem Gitter zur Simulation instationärer, zweidimensionaler, chemisch reagierender Strömungen, Diplomarbeit Institut für Allgemeine Mechanik, Aachen, 1992.
[35] E.S. Oran, J.P. Boris, Detailed modeling of combustion systems, Prog. Energy Combust. Sci. 7 (1981) 1–72.
[36] J.O. Hirschfelder, C.F. Curtiss, Theory of propagation of flames. Part I: general equations, in: Third Symposium on Combustion and Flame and Explosion Phenomena, Williams and Wilkins Co., Baltimore, 1949, pp. 121–127.
[37] R.J. Kee, J. Warnatz, J.A. Miller, A FORTRAN Computer Code Package for the evaluation of gas-phase viscosities, conductivities, and diffusion coefficients, Technical Report Report SAND-8209, Sandia National Labs., 1983.
[38] J. Warnatz, Influence of transport models and boundary conditions on flame structure, in: N. Peters, J. Warnatz (Eds.), Numerical Methods in Flame Propagation, Vieweg Verlag, Braunschweig/Wiesbaden, 1982, pp. 87–111.
[39] T.P. Coffee, J.M. Heimerl, Transport algorithms for premixed, laminar steady-state flames, Combust. Flame 43 (1981) 273–289.